Spontaneous Neuronal Network Dynamics Reveal Circuit's Functional Adaptations for Behavior

Sebastián Alejo Romano, Thomas Pietri, Veronica Pérez-Schuster, Adrien Jouary, Mathieu Haudrechy, German Sumbre

To cite this version:

Sebastián Alejo Romano, Thomas Pietri, Veronica Pérez-Schuster, Adrien Jouary, Mathieu Haudrechy, et al.. Spontaneous Neuronal Network Dynamics Reveal Circuit's Functional Adaptations for Behavior. Neuron, 2015, ⟨10.1016/j.neuron.2015.01.027⟩. ⟨hal-01523783⟩

HAL Id: hal-01523783
https://hal.science/hal-01523783v1

Submitted on 18 May 2017

Article

Neuron

Spontaneous Neuronal Network Dynamics Reveal Circuit's Functional Adaptations for Behavior

Highlights

- Spontaneous functional assemblies reflect the tectal retinotopic map
- Assemblies can be spontaneously engaged independently of retinal drive
- Assemblies are all-or-none preferred states shaped by inhibitory competition
- Assemblies are tuned to features relevant for a tectal-dependent vital behavior

Authors

Sebastián A. Romano,
Thomas Pietri, ..., Mathieu Haudrechy,
Germán Sumbre

Correspondence

sumbre@biologie.ens.fr

In Brief

The brain spontaneously produces activity patterns. Romano et al. show that this ongoing activity in a sensory brain area reflects neuronal mechanisms that assure robust circuit functioning for the extraction of behaviorally relevant sensory information.

Romano et al., 2015, Neuron *85*, 1070–1085
March 4, 2015 ©2015 The Authors
http://dx.doi.org/10.1016/j.neuron.2015.01.027

CellPress

Neuron
Article

Spontaneous Neuronal Network Dynamics Reveal Circuit's Functional Adaptations for Behavior

Sebastián A. Romano,[1,2,3] Thomas Pietri,[1,2,3] Verónica Pérez-Schuster,[1,2,3] Adrien Jouary,[1,2,3] Mathieu Haudrechy,[1,2,3] and Germán Sumbre[1,2,3,*]
[1]Ecole Normale Supérieure, Institut de Biologie de l'ENS IBENS, 75005 Paris, France
[2]INSERM, U1024, 75005 Paris, France
[3]CNRS, UMR 8197, 75005 Paris, France
*Correspondence: sumbre@biologie.ens.fr
http://dx.doi.org/10.1016/j.neuron.2015.01.027

SUMMARY

Spontaneous neuronal activity is spatiotemporally structured, influencing brain computations. Nevertheless, the neuronal interactions underlying these spontaneous activity patterns, and their biological relevance, remain elusive. Here, we addressed these questions using two-photon calcium imaging of intact zebrafish larvae to monitor the neuron-to-neuron spontaneous activity fine structure in the tectum, a region involved in visual spatial detection. Spontaneous activity was organized in topographically compact assemblies, grouping functionally similar neurons rather than merely neighboring ones, reflecting the tectal retinotopic map despite being independent of retinal drive. Assemblies represent all-or-none-like sub-networks shaped by competitive dynamics, mechanisms advantageous for visual detection in noisy natural environments. Notably, assemblies were tuned to the same angular sizes and spatial positions as prey-detection performance in behavioral assays, and their spontaneous activation predicted directional tail movements. Therefore, structured spontaneous activity represents "preferred" network states, tuned to behaviorally relevant features, emerging from the circuit's intrinsic non-linear dynamics, adapted for its functional role.

INTRODUCTION

In order to understand how the brain interacts with the external physical world, we should first understand its intrinsic dynamics by studying activity under conditions of minimal sensory drive (Deco et al., 2013; Ringach, 2009). Indeed, in the absence of stimulation, sensory brain areas remain highly active. This ongoing spontaneous activity consumes most of the brain's energy budget (Tomasi et al., 2013), and yet it has traditionally been considered as independent biophysical noise with no functional value for brain computations (Faisal et al., 2008; Shadlen and Newsome, 1998; Treisman, 1964).

However, several studies have emphasized the complex interaction between spontaneous activity and sensory-induced neuronal responses (Deco et al., 2011; Destexhe, 2011; Harris and Thiele, 2011; Ringach, 2009). They showed that the emergence of spontaneous activity patterns in sensory brain regions partially accounts for the across-trial variability observed in neuronal responses induced by identical sensory stimulation. Specifically, ongoing spontaneous activity can linearly sum with sensory input (Arieli et al., 1996; Azouz and Gray, 1999), inhibit and spatiotemporally confine sensory-induced responses (Petersen et al., 2003), or even non-linearly gate them (Luczak et al., 2013).

Furthermore, in recent years it was shown that spontaneous activity is spatiotemporally structured at a coarse level, according to the inter-regional brain circuitry of mice (Mohajerani et al., 2013) and humans (Fox et al., 2005; Raichle et al., 2001) and to the orientation column maps in the visual cortex of anesthetized cats (Kenet et al., 2003; Tsodyks et al., 1999). This suggests that spontaneous activity dynamically engages in coordinated network states affecting brain processing. The prevalence of spontaneous activity structure was further supported by the observation that spontaneous mean pair-wise spatiotemporal correlograms of multi-unit recordings from the ferret's primary visual cortex were only mildly modulated by sensory inputs (Fiser et al., 2004). Moreover, the spontaneous activity structure is clearly dependent on brain state (Harris and Thiele, 2011; Luczak et al., 2009) and samples a constrained repertoire of possible neuronal responses (Luczak et al., 2009), molded by experience (Berkes et al., 2011; Han et al., 2008; Sumbre et al., 2008). Finally, the awake rodent neocortical and hippocampal neuronal networks spontaneously replay fragments of previous sensory experiences, probably contributing to higher cognitive processes like memory, learning, and priming (Carr et al., 2011; Han et al., 2008; Ringach, 2009). Despite these advances, the neuronal interactions underlying the emergence of these spontaneous patterns remain largely unexplored (apart from theoretical approaches: Deco et al., 2011, 2013; Goldberg et al., 2004), and their biological significance with respect to neuronal circuits' behavioral roles is still unresolved.

In the present work, we addressed these two open questions by monitoring the spontaneous dynamics of the zebrafish larva optic tectum. The vertebrate optic tectum, analogous to the mammalian superior colliculus, contains functional sensory maps of the external world, and it is involved in spatial detection, attention, and the generation of commands for orienting motor behaviors (Krauzlis et al., 2013). In zebrafish, the tectum is the most complex layered brain structure and is essential for visually guided prey detection and capture (Gahtan et al., 2005). We monitored spontaneous activity by means of two-photon Ca^{2+} imaging of a significant fraction (~15%) of the optic tectum with cellular resolution in intact, non-anaesthetized, non-paralyzed zebrafish larvae expressing pan-neuronally the genetically encoded calcium indicator GCaMP3 (Tian et al., 2009). This technique enabled a systematic high-resolution description of the in vivo dynamics of large neuronal circuits (Ahrens et al., 2012; Orger et al., 2008; Sumbre et al., 2008). We thus studied the structure of tectal spontaneous neuronal activity within the context of optic tectum's functional role in vital behaviors (Gahtan et al., 2005; Niell and Smith, 2005).

We report that this spontaneous structure is organized in distinct neuronal assemblies of similarly tuned neurons, reproducing the tectum's retinotopic-like map even in the absence of retinal drive. Furthermore, we demonstrated an interplay of non-linear cooperative and competitive neuronal tectal dynamics suited for promoting the emergence of these spontaneous patterns. Finally, the spontaneous activity structure was associated with spontaneous tail flips, and it was particularly tuned to visual features that corresponded to larva's behavioral preferences during prey-capture assays, thus arguing for its biological relevance.

RESULTS

Visual Functional Maps of the Tectum

To study the optic tectum's spontaneous activity within the frame of the tectal role in vision processing (Gahtan et al., 2005; Krauzlis et al., 2013; Niell and Smith, 2005), we first characterized the tectum's visually induced responses in terms of stimulus spatial localization and stimulus movement direction. For this purpose, we presented to the larva light spots at different positions in the visual field and light bars moving in each of the four cardinal directions while simultaneously recording the activity of hundreds of neurons in the dorsal sensory layers of the tectum's *stratum periventriculare* (*SPV*; 836 ± 97 neurons from both tectal hemispheres of 8 dpf larvae, 14 larvae; Figures 1A and 1B).

In zebrafish, tectal neurons receive massive organized inputs from retinal ganglion cells (RGCs), exclusively from the contralateral eye, that synapse on the tectal neuropil creating a functional retinotopic tectal map of the contralateral visual field (Burrill and Easter, 1994; Niell and Smith, 2005). The contralateral dorsal and ventral visual hemifields are represented in the dorso-ventral tectal axis, whereas the nasal and temporal hemifields are mapped in the rostro-caudal tectal axis. Light spots presented at different positions in the visual field evoked activations (Ca^{2+}-induced significant relative change in fluorescence, $\Delta F/F$; Supplemental Experimental Procedures; Figures 1C and S1) of distinct neuronal groups (neuronal populations that consistently responded to a given stimulus across trials). According to these visual responses, we estimated the neuronal spatial tuning curves (their receptive field along the azimuthal position; Figure 1D). Central positions of the visual field activated rostral neuronal groups, and lateral positions activated more caudal ones, in agreement with previous studies (Niell and Smith, 2005) (Figures 1E and 1F). To enable comparisons across experiments, we summarized the tectal activation profiles across larvae by representing neuronal topographical positions in anatomically normalized tectal coordinates. Within a given optical plane, the tectal neuroanatomy possesses two functionally relevant axes: the rostro-caudal and the medio-lateral (see traces in Figure 1B). We therefore projected and normalized the Cartesian neuronal position coordinates on these axes (Supplemental Experimental Procedures). We observed that the contralateral visual field azimuth was represented along the tectal rostro-caudal axis (Figure 1G), revealing a tectal functional retinotopic map robustly conserved across different larvae.

Direction-selective neurons in the larval zebrafish *SPV* tectal layer have already been reported (Gebhardt et al., 2013), but their precise topographic arrangement is still unknown. In contrast to the functional topographic arrangement of neurons with spatial tuning (Figure 1G), direction-selective neurons (Figure 2A) were scattered across the tectal network without showing any clear topographic organization (Figures 2B and 2C).

Having systematically assessed neuronal tunings for visual object localization and movement direction, we then studied tectal spontaneous network activity within the framework of these functional roles.

Spontaneous Activation of Visual Representations

To study spontaneous activity in the tectum's sensory visual layers, we analyzed the dynamics of neuronal populations for periods of 1 hr, in the absence of sensory stimulation. Neuronal populations showed sparse basal activity, with low average neuronal activation frequencies (0.016 ± 0.015 Hz), with less than ~1% of the imaged population simultaneously active. Nevertheless, we observed significant pair-wise temporal correlations (Figure 3A) and frequent episodes of transient synchronous activations across neuronal subsets consisting of 2%–10% of the total population (Figure 3B), revealing concerted spontaneous neuronal dynamics.

We then asked if the patterns of these episodic spontaneous activations resembled, with single-neuron precision, those induced by visual stimulation (Figures 1 and 2). For this purpose, we calculated a matching index (MI; Supplemental Experimental Procedures) expressing the moment-to-moment degree of neuronal overlap between two given activation patterns (Hilgetag et al., 2002), in this case between spontaneous network dynamics (the spontaneous activation patterns) and the visually induced neuronal responses (i.e., neuronal groups). Significant MIs of light-spot-induced neuronal groups emerged transiently during the spontaneous activity (Figure 3C; 1.46 ± 1.79 episodes per min, or 0.23 ± 0.25 episodes per min for a given neuronal group) with MI levels comparable to those induced by light-spot stimulation (Figure 3E; mean MI of 0.23 ± 0.05 for spontaneous assemblies and 0.29 ± 0.09 for stimulations). To estimate the significance of these matches, we shuffled the neurons' spontaneous spike times. This disruption of the temporal neuronal dynamics completely suppressed the emergence of significant MIs, thus arguing for the significance of the observed spontaneous patterns that matched the visually induced responses (Figure 3F). Moreover, we failed to observe significant

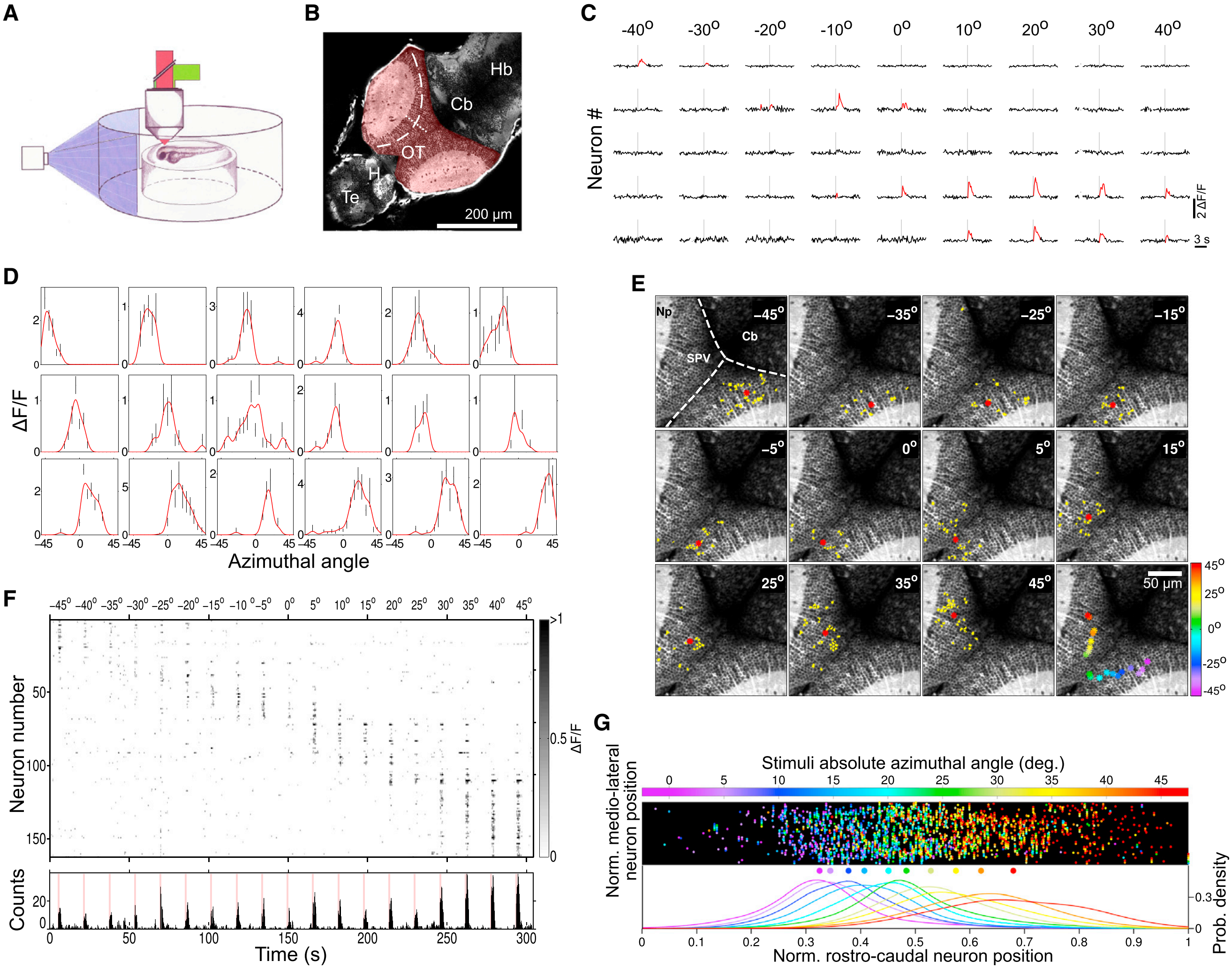

Figure 1. The Zebrafish Optic Tectum Contains a Functional Retinotopic Map

(A) Agarose-embedded 8 dpf zebrafish larvae were placed on an elevated stage, within a cylindrical recording chamber, and visually stimulated using a pico-projector. Spontaneous and visually induced neuronal activities were monitored by two-photon calcium imaging.

(B) An optical section of a larva's brain pan-neuronally expressing GCaMP3 (*HuC:GCaMP3*). The optic tectum is highlighted in red. The rostro-caudal and medio-lateral axes of the right tectum are schematically outlined by dashed and pointed lines, respectively. Cb, cerebellum; H, habenula; Hb, hindbrain; OT, optic tectum; Te, telencephalon.

(C) Typical single-trial neuronal *ΔF/F* traces induced by 1 s visual stimulation with 4° light spots. Vertical gray line: stimulus onset. Stimulus azimuthal positions are indicated at each stimulation onset (0°, negative and positive angle values represent frontal, right, and left visual field positions, respectively). Significant *ΔF/F* transients are highlighted in red. Breaks in the traces are discarded frames due to movement artifacts.

(D) Representative neuronal spatial tuning curves (red line). Mean ± SD of neuronal responses are shown in black.

(E) Topography examples of neuronal groups consistently activated by light spots at the azimuth angles indicated in the top right corner. Activated neurons are colored in yellow, and the neuronal groups' centroids are depicted as red asterisks. Bottom right: the neuronal group centroids color coded according to the azimuth angle (color bar on the right). As expected from a retinotopic map, a continuous progression of centroids along the contra-lateral rostro-caudal axis is clearly observed. Top left: anatomical landmarks. Dashed lines delineate the tectal-cerebellar and inter-hemispheric tectal boundaries. Cb, cerebellum; Np, tectal neuropil; SPV, tectal somatic periventricular layer.

(F) Raster plot of *ΔF/F* responses presented in (E). Grayscale, *ΔF/F* amplitude. Top labels indicate the light-spot azimuth angle. For visualization purposes, we show trials rearranged according to azimuth angle (during experiments, they were presented in random order). Only responsive neurons are shown. Bottom: histogram of the neuronal Ca^{2+} transients. Red bars mark light-spot stimulation periods.

(G) Normalized topography of neuronal groups induced by 4° light-spot stimulation experiments (n = 9). Each point in the upper panel represents the normalized position of a visually activated neuron, whose color indicates the absolute azimuth angle of the stimulating light spot (color bar on top). Bottom: probability density distributions of the normalized rostro-caudal neuron positions according to the stimulus position. Distributions are color coded according to the top color bar. Dots represent the medians. The smooth progression of the latter reflects a robust tectal retinotopic map conserved across larvae.

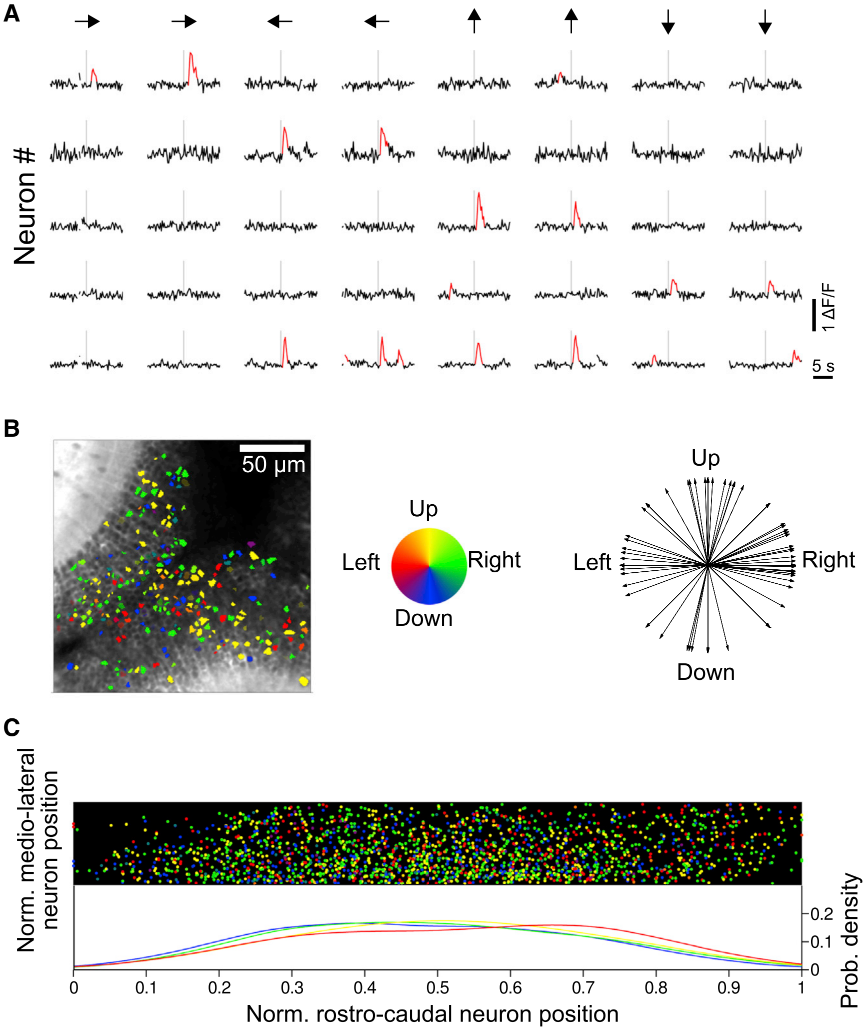

Figure 2. Direction-Selective Tectal Neurons Are Topographically Scattered

(A) Typical single-trial neuronal *ΔF/F* responses induced by moving light bars. Vertical gray line marks stimulus onset. Arrows indicate bar moving direction. Significant *ΔF/F* transients are highlighted in red.

(B) Left: example of the topography of direction-selective neurons. Neurons are colored according to their direction selectivity (color wheel). Right: neuronal direction preferences of this example.

(C) Normalized topography of neuronal groups induced by direction-selectivity experiments (n = 14). Each point in the upper panel represents the normalized position of a direction-selective neuron whose color indicates its direction selectivity (same color code as that in B). Bottom: color-coded probability density distributions of the normalized rostro-caudal position of direction-selective neurons. The similarity between the distributions indicates the lack of direction-selective topographic arrangement in the tectum.

spontaneous MIs of direction-selective neuronal groups (Figures 3D and 3F). These results suggest that certain spontaneous tectal activity patterns matched, with significant cellular precision, transient network states that corresponded to spatially localized visual representations.

The Spatiotemporal Structure of Spontaneous Activity

Both the emergence of spontaneous activation patterns resembling visual representations and the presence of significant spontaneous neuronal pair-wise correlations (Figure 3) motivated us to look for dynamical neuronal assemblies, i.e., groups of neurons showing significantly correlated spontaneous activities. For this purpose, we combined and adapted previously proposed dimensionality reduction and clustering methods (Lopes-dos-Santos et al., 2011; Peyrache et al., 2010; see Supplemental Experimental Procedures for details; Figures S2A–S2C). This combined technique markedly outperformed other widely used algorithms such as k-means or hierarchical clustering, as measured by cluster validation tests (Figures S2D–S2I).

Using this PCA-promax technique, we identified distinct assemblies composed, in most cases, of neighboring neurons (Figures 4A–4D). During the 1-hr experiments, we observed the emergence of 47 ± 19 spontaneous unique assemblies with a rate of 2.4 ± 0.9 per min and comprising 25 ± 9 neurons per assembly (average ± SD; Figure 4A). The spontaneous assemblies consisted of significantly temporally correlated neurons (Figure 4C), representing 80% ± 19% of the significant neuronal pair-wise correlations observed in the tectal population (Figure 4B). We therefore concluded that these assemblies accounted for a large fraction of the correlational structure of the entire imaged neuronal population.

We quantified the assemblies' features by the implementation of several normalized dimensionless indexes that enabled us to unbiasedly compare across experiments. To infer the significance of the measured properties of the assemblies, we controlled against sets of shuffled surrogate assemblies (null models). For this purpose, we first shuffled neuronal identities by permuting the indexing of the neuronal population. Then, we built the null models by grouping neurons according to the original assemblies, but using the permuted neuronal indexing. This was repeated for 1,000 rounds, creating a null model set of mock random clusters with randomized topographies, conserving the rest of the statistics in the data (firing rates, pair-wise correlations, etc.). This allowed us to test for the significance of the original assemblies' features, with respect to the shuffled clusters.

Using this approach, we observed that spontaneous assemblies were mostly constrained to either tectal hemisphere (71% of them were significantly unilateral, laterality index > 0.74, $p < 0.05$, where 0 corresponds to an assembly whose neurons are equally distributed across hemispheres, and 1 indicates a completely unilateral arrangement). Moreover, 51% showed

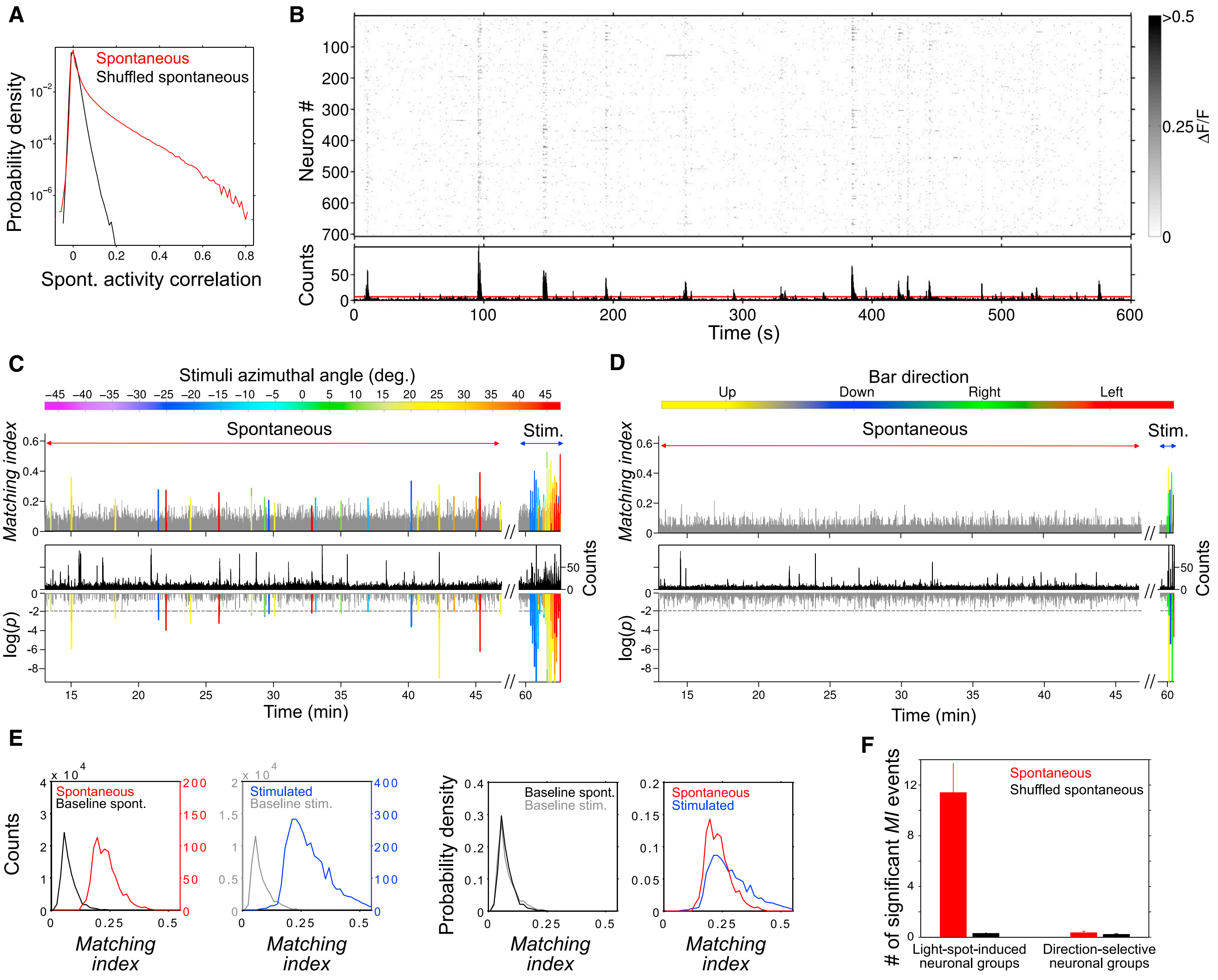

Figure 3. Visual Spatial Representations Spontaneously Emerge in the Absence of Sensory Stimulation

(A) Probability density distribution of pair-wise spontaneous neuronal activity correlations (red, Pearson linear coefficient, *r*) observed across experiments (n = 23). Only significant *ΔF/F* transients were considered. In black is the same distribution after neuronal interactivation interval shuffling (IAI) that destroys temporal coordination across neurons. 16% of neuronal pairs showed correlations that could not be explained by the latter distribution (*r* = 0.07 ± 0.06, $p < 0.05$).

(B) Example of a raster plot of spontaneous Ca^{2+} transients, revealing episodes of synchronous activations. Grayscale: *ΔF/F* amplitude. Bottom: histogram of the Ca^{2+} transients. The red line marks the threshold for significant population events.

(C and D) The degree of match between spontaneous network activations and the visually induced neuronal groups quantified by the matching index (MI), ranging between 0 and 1, corresponding to null and full match, respectively. (C) Top: example of MI dynamics for matches to neuronal groups induced by 4° light spots during stimulated and spontaneous activity periods (blue and red two-headed arrows, respectively). Significant MI peaks are colored according to the angular position they represent (the stimulus position that induced the activation of the neuronal group that best matched the spontaneous activation pattern; top color bar). Non-significant matches are shown in gray. For visualization purposes, we show trials with stimulation angles in increasing order. Bottom: corresponding population histogram of the neuronal Ca^{2+} transients (top, black) and the base 10 logarithm of the MI p values (bottom). MI peaks with p value < 0.01 (99% confidence; dashed gray line; see Supplemental Experimental Procedures) are considered significant and colored as in top panel. (D) Same as (C), but for direction-selective neuronal groups. Notice the absence of significant spontaneous activations.

(E) Left to right, count histograms of significant spontaneous (red) and stimulated (blue) MIs and the corresponding non-significant MI baselines (black and gray), and probability density distributions comparing these baselines and the significant MIs. Note the comparable magnitudes of spontaneous and stimulated significant MI events.

(F) Average number of significant MI events of visually evoked neuronal groups during spontaneous activities, per experiment, per neuronal group (red), for light-spot-induced (left) and direction-selective (right) neuronal groups. The number of significant events for these neuronal groups during IAI-shuffled spontaneous activities is shown in black.

significant topographical compactness (Figures 4D and S7B; compactness index > 0.46, $p < 0.05$, ranging between 0 and 1, quantifying the spatial tightness of the assembly; see Figures S5A and S5C for compactness index examples and calculation). The centroids of spontaneous assemblies were arranged in a continuous progression along the rostro-caudal tectal axis, both in pooled (Figure 4F) and individual experiments (top panels in Figure 4G), and the normalized rostro-caudal neuron positions linearly predicted the normalized rostro-caudal centroid positions of the assemblies to which they belong (Figure 4E; $r = 0.7$, $p < 10^{-5}$, explaining 49% of the variance), thus demonstrating that neighboring neurons tend to have spontaneously correlated activity. In contrast, we did not find such arrangement across opposite hemispheres (Figures S3A and S3B), suggesting no topographic organization according to the inter-hemispheric spontaneous correlations. These results imply that spontaneous assemblies tend to be formed by neighboring neurons of the same tectal hemisphere, often resulting in topographically compact neuronal clusters.

Interestingly, light-spot-induced and spontaneous assemblies within the same hemisphere displayed comparable topographical arrangements (compare top and bottom panels in Figure 4G and Figure S3C; light-spot-induced assemblies were defined through the previously used PCA-promax procedure).

We found that neuronal pairs with similar spatial tuning curves tended to show higher spontaneous correlations, while this was not true for direction preference similarity (Figure 4H). Accordingly, spontaneous assemblies had a significant bias to regroup neurons with similar spatial tuning curves, when compared to the shuffled null models (top panel in Figure 4I; $p < 10^{-5}$ for tuning curve correlation coefficients > 0.25, not explained by the null model). We then asked if this result could be explained solely by a combination of a retinotopic map and the usually observed tendency for higher spontaneous correlations between nearby neurons (Kerr et al., 2007; Smith and Kohn, 2008). To test this possibility, we built an additional set of null models with the additional constraint of conserving the relative pair-wise physical distances between neurons found in the original assemblies (topographical null models; Figure 4J). This method enabled us to destroy the functional specificity of the assemblies while keeping intact their topographic compactness and the tectum's retinotopic map. Remarkably, despite the preservation of the distribution of pair-wise distances, the original assemblies still had a significant bias toward neurons with similar tunings, when compared to these null models (bottom panel in Figure 4I). Nor could topographical null models of light-spot-induced neuronal groups completely explain the transient spontaneous emergence of spatially localized visual representations (Figure S3D). Therefore, spontaneous assemblies do not simply derive from the coarse law of increase in pair-wise spontaneous correlations with decrease in inter-neuronal distance. On the contrary, there is a clear specificity in the composition of spontaneous neuronal assemblies such that they grouped functionally related neurons rather than exclusively neighboring ones. In agreement with these results, spontaneous correlations were related to the neuronal signal correlations (the pair-wise correlations of the mean neuronal responses to an ensemble of stimuli). But notably, noise correlations (the pair-wise correlations of trial-to-trial variability in neuronal responses) were also significantly associated with the spontaneous correlations (Figure S4H). This suggests that the fluctuations of neuronal responses across trials are related to the neuronal interactions represented in the spontaneous tectal assemblies. On the other hand, spontaneous assemblies were not significantly composed of similar direction-selective neurons, and therefore the assemblies were not directionally tuned, when compared to null models ($p > 0.05$; Figures S3E–S3G). These results suggest that the fine local topographic structure of the tectal functional retinotopic map, but not the directional map, can be reconstructed from the dynamics of the tectal spontaneous activity.

Importantly, the similarity between population neuronal dynamics during spontaneous and visually induced activity was also supported by other methods completely independent of PCA and promax. First, multidimensional scaling (MDS), allowed for a qualitative validation of the global structure of spontaneous and induced neuronal population dynamics (Figures S4A–S4E). We then estimated that spontaneous neuronal assemblies explained the clusters of neurons with correlated light-spot-induced responses with only ~10% error (Figures S4F and S4G; Supplemental Experimental Procedures).

Therefore, tectal spontaneous neuronal activity is organized in dynamic assemblies mostly resembling neuronal response patterns induced by spatially localized visual stimuli. This suggests that structured tectal spontaneous activity is tightly associated with the functional role of the tectum in visual spatial detection.

Spontaneous Assemblies Do Not Reflect Retinal Inputs

To test whether the topographical organization of tectal spontaneous assemblies resulted from structured inputs arriving from the retina (the vast majority of the tectal afferents; Burrill and Easter, 1994), we performed unilateral retinal ablations or eye enucleations 1–3 days before the experiments. Since the retina projects only to the contralateral tectum, we could perform the experiment and its control in the same larva. Both retinal-input-deprived (*RID*) tecti and their control tecti displayed spontaneous assemblies in a continuous topographical arrangement along the rostro-caudal tectal axis, indicating that we could reconstruct the functional retinotopic map from the spontaneous activity, even in the absence of retinal inputs (Figures 5A–5D; the neuron's position linearly predicted the assembly's centroid position for both *RID* and control tecti, $r = 0.6$ and $r = 0.74$, respectively). Compared to normal tecti, neurons in the deprived tecti were spontaneously active at similar levels (control $\Delta F/F$: 0.58 ± 0.2; deprived $\Delta F/F$: 0.59 ± 0.19; $p = 0.055$), yet at slightly lower frequencies (control: 0.03 ± 0.04 Hz; deprived: 0.029 ± 0.03 Hz; $p = 0.005$) and mildly longer durations (control: 0.51 ± 0.21 s; deprived: 0.49 ± 0.24 s; $p < 10^{-5}$) (Figures S6A–S6C). Assemblies within the deprived tecti spread over similar areas (control: 0.28 ± 0.16; deprived: 0.31 ± 0.19; $p = 0.67$) but were less compact with respect to those found in the normal tecti (control: 0.61 ± 0.18; deprived: 0.5 ± 0.14; $p < 10^{-5}$) (Figures S6D and S6E). This difference in compactness could be explained by shuffling ~25% of the neuronal composition of normal tecti assemblies (Figure 5E; $p < 0.01$). Therefore, this indicates that spontaneous assemblies of the optic tectum (the

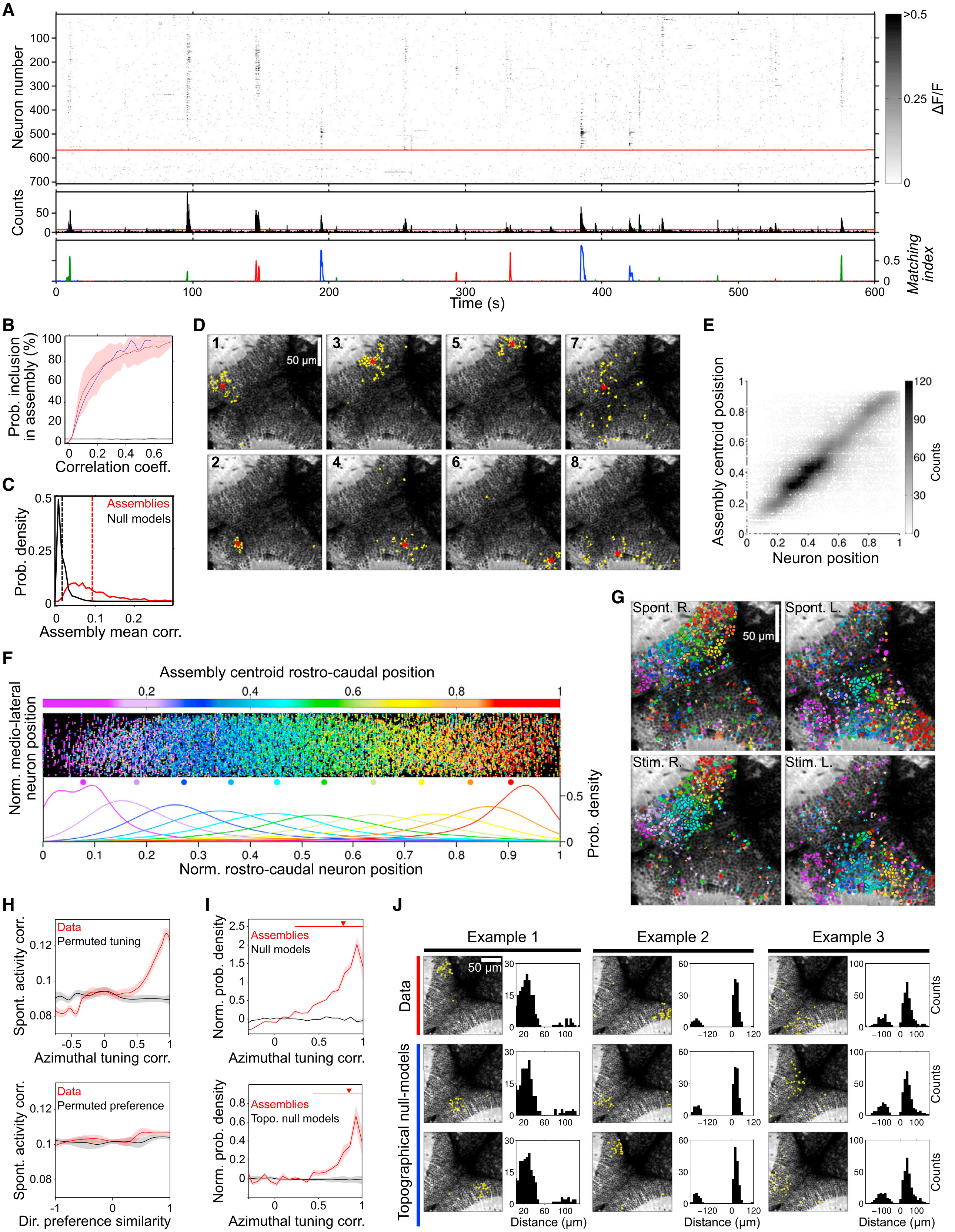

(legend on next page)

major retino-recipient brain region in zebrafish) are not the simple outcome of correlated feed-forward inputs arriving from the retina.

Spontaneous Assemblies Represent Preferred Network States

To study the dynamic principles underlying the emergence of spontaneous assemblies, we analyzed how the spontaneous coordinated activations of the neurons within an assembly affected the activity of the assembly's neurons. For this purpose, we calculated the activation probability of neurons (i.e., the fraction of imaging frames in which the neuron was active) within a given assembly, as a function of the correlation between the instantaneous activity pattern of the tectal population and the topography of the assembly being tested (the latter correlation indicated how well the spontaneous activity at any given moment matched the spontaneous assembly being studied). The obtained activation/correlation profiles showed strong activation probabilities ("facilitations") that sharply increased as the spontaneous activity pattern gradually resembled the topography of the tested assembly. This implies that the spontaneous neuronal assembly patterns represent network states that are "preferred" by the assembly neurons, since these neurons are markedly more prone to be activated when the spontaneous network activation better resembles the pattern of the assembly they belong to (up to an ~40-fold increase compared to the null model; Figures 6A, 6B, and S7A). The upper-third most-steep "facilitations" showed step-like activation profiles capable of producing an all-or-nothing-like effect, while the other two-thirds showed more gradual, rather linear, "facilitations." This result suggests that the dynamics of assembly neurons is capable of abruptly switching from sparse weak to fully correlated activations.

Interestingly, assemblies showing step-like activations were more topographically compact (Figure S7B; compactness index, step-like group: 0.61 ± 0.18; linear group: 0.5 ± 0.17; $p < 10^{-5}$), and their spatial receptive fields were better tuned than the linear ones (Figure S7C; average assembly normalized tuning peak of 10.1 ± 6.0 for step-like assemblies and 7.7 ± 5.0 for linear assemblies, $p = 10^{-5}$). Thus, this suggested that spontaneous assemblies with all-or-nothing-like activations carried more information about visual spatial representations than assemblies with linear ones.

These results imply that tectal spontaneous assemblies are stable "preferred," coherently tuned network states, entrained by a non-linear synergistic interaction between assembly neurons.

Tectal Assemblies Show Biased Competitive Dynamics

To investigate the principles underlying the delineation of the compact topography of the neuronal assemblies, we tested whether the tectal assemblies are subjected to inter-assembly inhibitory competition. To this end, we simultaneously presented to one of the larva's eyes two 4° light spots (angular separation: $\Delta 10^\circ$–$\Delta 30^\circ$) while monitoring neuronal activations of the contralateral tectum. We observed that simultaneous-light-spot stimuli induced neuronal responses of lower magnitude (in terms of

Figure 4. Spontaneous Emergence of a Retinotopic-like Map from the Dynamics of the Ongoing Neuronal Activities

(A) Same raster plot and histogram as in Figure 3B, with neurons sorted according to the assemblies obtained with PCA/*promax*, allowing the visualization of distinct neuronal assemblies. Neurons not assigned to any assembly lie below the red line. Bottom: example of the MI dynamics for three representative spontaneous assemblies (red, green, and blue). Note that each MI peak of the same color corresponds to the activation of roughly the same group of neurons.

(B) Probability of inclusion of a neuronal pair in a spontaneous assembly, as a function of their pair-wise spontaneous activity correlation coefficient, averaged across experiments (red), and for the experiment presented in (A) (blue). The same calculation for shuffled sets of surrogate assemblies (null models) is presented in black. Error bars, SD across experiments.

(C) Probability density distribution of the mean pair-wise spontaneous activity correlation coefficient of neurons within each of the spontaneous assemblies (red). The same distribution for null models is presented in black. Dashed lines: the distributions' means (0.09 ± 0.06 for spontaneous assemblies and 0.01 ± 0.01 for null models; means and SD $p < 10^{-5}$).

(D) Topographies of eight examples of spontaneous neuronal assemblies. Assembly neurons are labeled in yellow. Red asterisks: assembly centroids. 1–6: typical compact assemblies. 7–8: sparse assemblies.

(E) Density plot of the normalized rostro-caudal position of each neuron against the normalized rostro-caudal centroid position of its spontaneous assemblies. Grayscale: data count.

(F) Normalized topography of spontaneous assemblies across larvae (n = 23). Top: each point represents the normalized position of a neuron participating in a spontaneous assembly whose color indicates the normalized rostro-caudal centroid positions of its assemblies (color bar on top). Bottom: probability density distributions of the normalized rostro-caudal position of neurons for assemblies within the same range of colors (for ten bins of the color bar). Colored dots: the medians for each distribution curve.

(G) Spontaneously emerging retinotopic-like map in one typical experiment. Spont., all the spontaneous assemblies whose centroids lay on the right (R.) and left (L.) tecti. Neurons belonging to assemblies with similar topographic centroids were similarly colored. The colors represent the average normalized rostro-caudal centroid position of their assemblies. The transparency represents the SD across centroids. Stim. L. and R.: the same representation for the light-spot-induced responses. Note the resemblance between Spont. and Stim. panels, showing a graded change in colors along the rostro-caudal axes.

(H) Top: local regression of significant pair-wise spontaneous neuronal activity correlation coefficients against the pair-wise neuronal spatial tuning curve correlation coefficients (red). The same regression after randomly permuting across neurons the neuronal tuning curves (black). Bottom: same as top, but regressing against neuronal directional preference similarity (red; pair-wise dot product of direction-preference vectors) and permuting neuronal directional preferences (black).

(I) Top: probability density distribution of the pooled pair-wise correlation coefficients of azimuthal tuning curves of neurons that are grouped by a spontaneous assembly (red). This distribution was normalized by dividing by the distribution resulting from null models. For comparison, we show in black the average normalized distribution for single null model runs. Note that spontaneous assemblies show a bias toward grouping neurons with highly similar tuning curves (significant bias range and median are indicated by top red line and arrowhead). Bottom: same as top, but after normalization with topographical null models. Lines and confidence interval in (H) and (I): average and jackknife procedure across experiments.

(J) Two examples of topographical null models (blue) of three spontaneous assemblies (red). Black bar histograms: the corresponding inter-neuron distance distributions (positive and negative distances correspond to intra- and inter-hemisphere neuronal pairs, respectively).

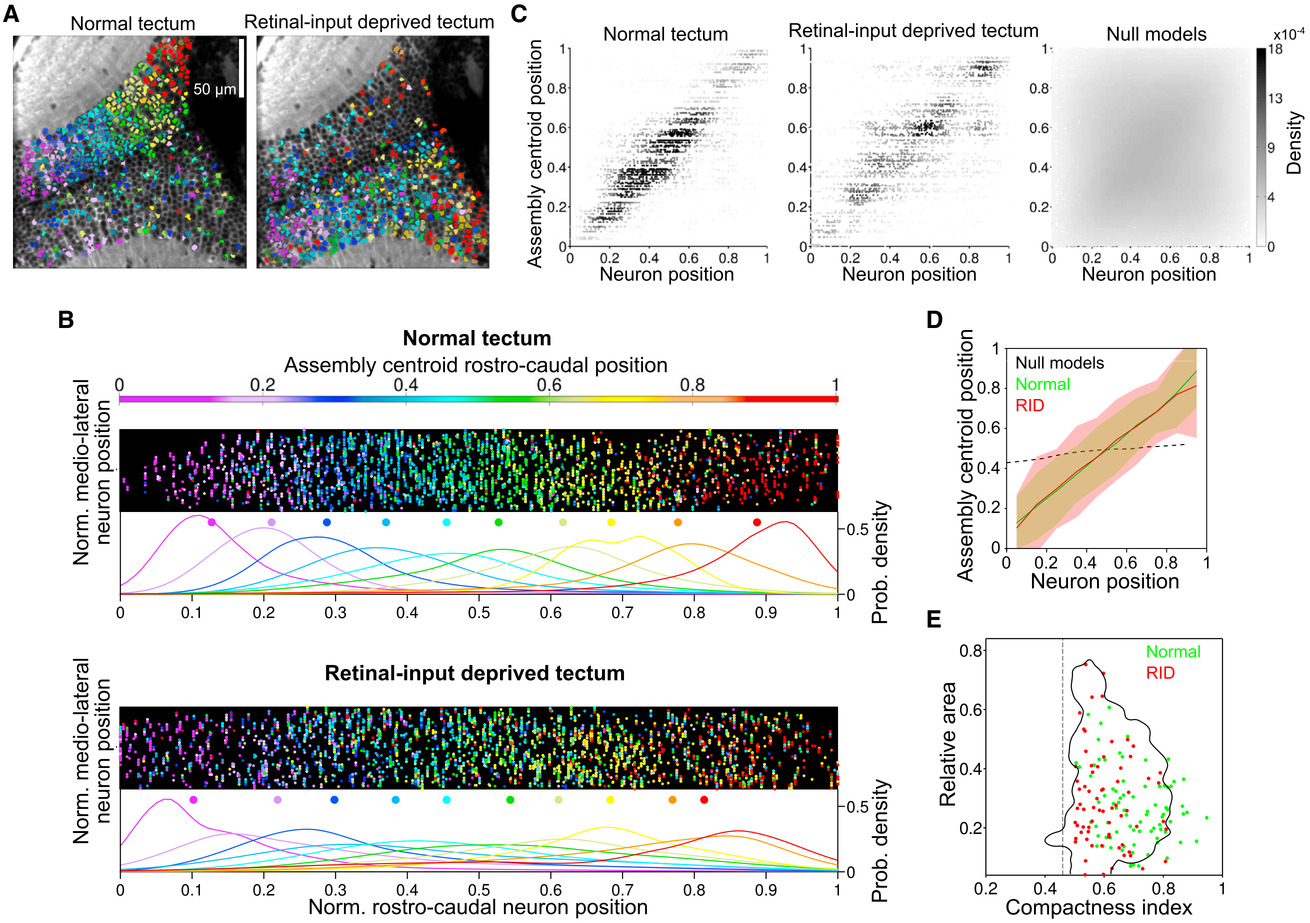

Figure 5. Spontaneous Assemblies Are Not Driven by Retino-Tectal Inputs

(A) Example of a spontaneously emerging retinotopic-like map 24 hr after retinal-input deprivation (*RID*) of the left tectum (right eye enucleation at 7 dpf). Spontaneous assemblies whose centroids lay on the normal and *RID* tectum are shown on the left and right panels, respectively. Data are represented as in Figure 4G.

(B) Normalized topography of spontaneous assemblies for normal (top) and *RID* (bottom) tecti (n = 5). Data are represented as in Figure 4F.

(C) Density plot of the normalized rostro-caudal position of each neuron against the normalized rostro-caudal centroid position of its spontaneous assemblies for both the normal (left) and *RID* tecti (middle) and for assemblies' null models (right). Grayscale: data density.

(D) Regression of the data shown in (C) for the normal (green) and RID (red) tecti (mean and 95% confidence interval). The dashed black line shows the regression result for null models.

(E) Relative area as a function of compactness index (see Supplemental Experimental Procedures) for spontaneous assemblies in the normal (green) and *RID* (red) tecti. Only significantly compact assemblies are shown (significance threshold indicated by dashed line). The black solid line outlines the region occupied by 99% of the normal tecti spontaneous assemblies with random 25% rearrangement of their neuronal composition. Spontaneous assemblies in *RID* tecti are not significantly different from this rearranged assembly population.

induced-responses amplitude and number of responsive neurons) than those induced by each of the two light spots presented individually (Figure 6C), suggesting that neuronal responses are affected by inhibitory interactions during the simultaneous stimulations. The lower-magnitude responses to the simultaneous-two-light-spot stimuli could be the result of a uniform inhibition across the whole tectal network. Alternatively, it may represent a specific competition between the neuronal groups induced by each light spot. Our results showed that simultaneous-light-spot trial responses did not represent a simple superposition of both individual-light-spot neuronal groups, but rather were biased toward one of these groups (Figures 6D and S7D). This suggests that the simultaneous presentation of two light spots did not induce a global uniform tectal inhibition, but instead represents competitive inhibitory interactions between the neuronal groups induced by each of the individual light spots.

To quantify this competition, we assessed the extent of the contribution of each of the two individual-light-spot neuronal representations to the explanation of the simultaneous-light-spot trial responses. To this end, we decomposed every trial response induced by a simultaneous light spot with respect to a weighted linear summation of two individual-light-spot-induced template patterns. These latter templates were estimated as the across-trial average responses to each individual light spot when presented separately (e.g., red and green bar plots in

Figure 6D; see Supplemental Experimental Procedures). Thus, to analyze the relative contributions of each individual-light-spot-induced neuronal group, for each trial of simultaneous stimulation we computed an imbalance index, defined as the difference between both template weights divided by their sum. This index ranges between -1 and 1, where 0 indicates exact balanced linear summation of the individual-light-spot average responses (no inhibitory interaction between the two neuronal groups), while 1 and -1, respectively, indicate that only the most rostral or the most caudal template was enough to explain the simultaneous-light-spot trial response (winner-takes-all interactions).

We observed competitive interactions between the neuronal groups that were not compatible with a balanced linear summation. In 70% of the experiments (14 out of 20), simultaneous-stimulation response trials were characterized by a neuronal group being more strongly activated (i.e., having a greater decomposition weight) than the other (examples in Figures 6E and S7E). To further characterize this phenomenon, we classified experiments in a data-driven manner (Figure S7F): (1) responses were dominated by the most rostral neuronal groups (30%); (2) dominated by the most caudal neuronal groups (20%); (3) alternating domination of either the rostral or caudal neuronal groups (20%); (4) balanced linear summation (20%) (Figure 6F).

These results demonstrate that the tectal functional assemblies are subjected to competition in 70% of the cases such that, when simultaneously engaged, the resulting activation pattern is biased toward one of the assemblies. We thus suggest that the spontaneous functional assemblies of the tectum are topographically delineated by this inter-assembly biased competitive dynamics.

Behavioral Correlate of the Tectum's Spontaneous Neuronal Assemblies

Since we found that spontaneous assemblies are related to the optic tectum's role in spatial vision, we thus further studied whether the assemblies' population spatial tuning reflected parameters pertinent to visually guided tectum-dependent behaviors. For this purpose, we compared the functional tuning (i.e., spatial and size tuning) of spontaneous assemblies with the larva's detection performance during prey-capture behavior.

We first studied how the larva's visual field is represented by the tectal spontaneous assemblies. For this, we estimated the receptive fields of the assemblies (the normalized sum of the spatial tuning curves of all the neurons within an assembly). To correct for uneven tectal representations of the visual field, we further divided the spontaneous assemblies' receptive fields by the average receptive field of shuffled null models, resulting in normalized assembly receptive fields independent of any potential sampling bias in the data (i.e., if a particular visual field position is represented by a considerably larger neuronal population than other positions). After this correction, we observed that spontaneous assemblies representing lateral position of the visual field had significantly narrower spatial tuning curves and showed significantly higher activation levels (*AL*, the overall integral of the MI) than those representing rostral positions (Figures 7A and 7B).

To assess this spontaneous lateral over-representation of the visual field with respect to the larva's behavior, we monitored larva behavior during prey-capture assays to evaluate their visual detection capabilities. Zebrafish larva's hunting behavior is mostly driven by vision and dependent on the tectum (Gahtan et al., 2005). It begins by detection of the prey followed by a sequence of discrete locomotor maneuvers, some of which are uniquely performed during hunting (Bianco et al., 2011; Gahtan et al., 2005; McElligott and O'malley, 2005). We filmed the behavior of zebrafish larvae (n = 60) in the presence of low-density *paramecia* using a high-speed video camera (200 Hz). We defined the instant of prey detection as the video frame preceding the onset of a prey-capture behavior. For all confirmed prey-capture behaviors, we measured the zebrafish-*paramecium* distances and relative angles at the moment of *paramecium* detection. The distribution of these relative angles showed a strong bias toward lateral positions of the visual field (Figure 7C). Remarkably, this larva's tendency to better detect *paramecia* at lateral angles matched the spontaneous assemblies' over-representation of the lateral visual field (Figure 7C).

We then asked if there was also a parallel between the angular tuning of spontaneous assemblies and the angular size of *paramecia* on the larva's retina at the moment of detection. From visually induced responses, we observed that light spots of 4° induced the activation of more compact and spatially constrained assemblies than those of 8° and 12° (Figure S5B; compactness indexes for 4°: 0.57 ± 0.18, 8°: 0.42 ± 0.15, 12°: 0.43 ± 0.17; 4° versus 8°: $p < 10^{-5}$, 4° versus 12°: $p < 10^{-5}$). Moreover, spontaneous assemblies better and more often matched neuronal groups activated by light spots of 4° compared to those induced by 8° and 12° light spots, as measured by activation density maps (Figure S5D; correlation between density maps of stimulated neuronal groups and their best-matching spontaneous assembly: 4°: 0.80 ± 0.13, 8°: 0.65 ± 0.18, 12°: 0.62 ± 0.19; 4° versus 8°: $p < 10^{-5}$, 4° versus 12°: $p < 10^{-5}$). This was also true when we quantified this similarity by the neuron-to-neuron topographical overlap between the visually induced neuronal groups and the spontaneous assemblies' patterns (inset in Figure 7E; as quantified by the matching index for the topographic overlap between these patterns, number of significant spontaneous MIs per stimulated neuronal group, per experiment, 4°: 0.25 ± 0.04, 8°: 0.09 ± 0.02; 12°: 0.07 ± 0.02; 4° versus 8°: $p = 0.003$, 4° versus 12°: $p = 10^{-5}$). Importantly, the significant pattern matches between spontaneous assemblies and neuronal groups induced by 4° light spots were comparable to those representing the inter-trial variability of the induced neuronal responses (Figure 7D). This suggests that the spontaneous assemblies were indistinguishable from the single-trial response patterns induced by 4° light spots. Remarkably, when we determined the angular size of *paramecia* on the larva's retina, at the moment of *paramecia* detection (Bianco et al., 2011; McElligott and O'malley, 2005), we observed that larvae most frequently initiated a prey-capture behavior when *paramecia* were at a distance corresponding to ~4°–5° on the larva's retina (Figure 7E).

Finally, we asked whether the spontaneous activation of a tectal assembly can be related to the generation of a behavioral output. For this purpose, we monitored spontaneous tectal

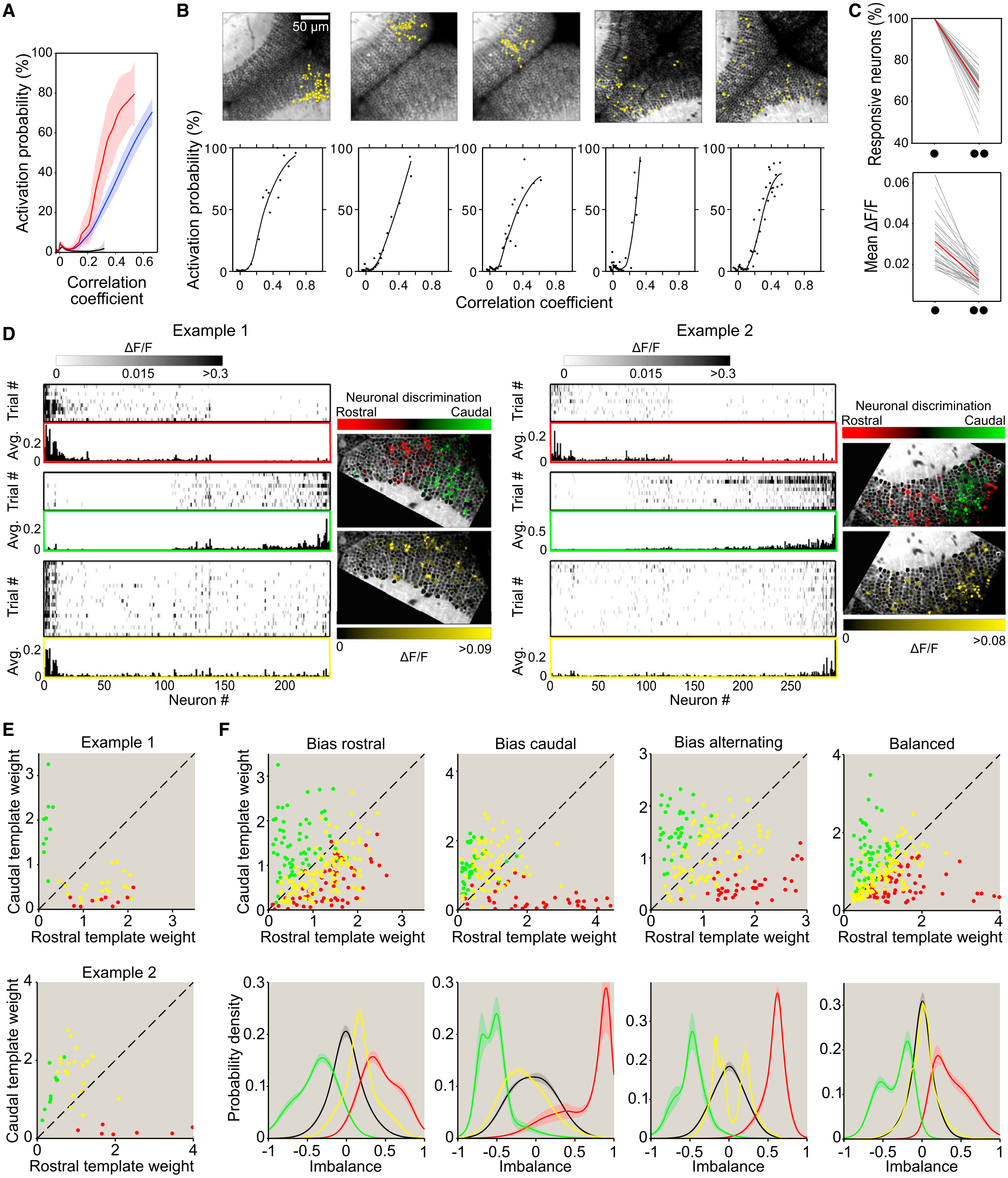

Figure 6. The Optic Tectum Shows Non-Linear Cooperative and Competitive Dynamics

(A) Activation probability of spontaneous assembly neurons as a function of the correlation between the assembly pattern and the spontaneous tectal network activity. Average activation probability "facilitation" profiles for the upper-third most-steep curves (red, non-linear step-like group) and for the rest of the curves (blue, linear group). As a control, the curves for null models are presented in black. Curves, regression fits across assemblies; confidence interval, SEs.

(legend continued on next page)

activities in head-restrained larvae so we could also monitor the spontaneous tail motor behaviors. Under this condition, larvae produced brief isolated episodes of tail movements (< 300 ms; 40 ± 14 episodes per hr). Remarkably, we observed that 11% of these spontaneous movement episodes (22 out of 199, 4.4 episodes per hr; n = 5) were immediately preceded by the spontaneous activation of a topographically compact tectal assembly (Figures 7F and S7G; compactness index = 0.74 ± 0.1). As a control, we used tectal spontaneous activations to predict the onset of tail movements of other larvae. Using this method, we found that only 0.2% of the movement episodes were preceded by compact tectal assemblies. Given the frequency of spontaneous assembly activations and tail movements, the probability of predicting 11% of the episodes by chance is in the order of 10^{-20}. Notably, when the activation of a spontaneous assembly preceded a tail flip with kinematics that indicated a turning movement (14 out of 22), in 93% of the cases the assembly corresponded to the contralateral tectal hemisphere (Figures 7F and S7G; 13 out of 14, 7 to each side; $p = 9 \times 10^{-4}$). We then calculated the probability of a tail movement onset during the imaging frame *i* as a function of the correlation between the tectal activity pattern at frame *i-1* and the patterns of all the spontaneous neuronal assemblies found. The latter correlation indicates how well the pattern of tectal activity preceding a tail flip matches the topographies of a spontaneous neuronal assembly. We observed a sharp step-like increase of this probability as the spontaneous tectal activity gradually matched the topography of a spontaneous assembly (Figure 7G).

In summary, these results indicate a behavioral correlate of spontaneous tectal assemblies and that these assemblies are particularly tuned to relevant visual information, paralleling behavioral performance observed in a vital tectum-dependent behavior (prey-tracking).

DISCUSSION

Contemporary theories of sensory perception regard the brain not as a stimulus-driven processor, but rather as an active system with rich intrinsic dynamics that interacts with environmental sensory information and the organism's internal states (Engel et al., 2001; Fiser et al., 2004; Harris, 2005; Ringach, 2009). Structured spontaneous brain activity in sensory brain areas is seen as a reflection of this phenomenon, and thus it should reveal features about the neuronal circuits' functional role.

We report, at the single-neuron level, that tectal spontaneous activity is significantly correlated (Figures 3A and 3B) and spatiotemporally organized in topographically compact assemblies of neurons with matching receptive fields (Figure 4). Although it might be expected that this result could reflect the combination of functional topography and the well-known tendency of nearby neurons to show higher spontaneous correlations (Kerr et al., 2007; Smith and Kohn, 2008), we further demonstrated that these assemblies do not simply assemble neighboring neurons, but showed significant specificity for functionally similar neurons (Figure 4I), resulting in coherently tuned subnetworks. Hence, these spontaneously engaging tectal assemblies are true functional neuronal assemblies.

We further assessed the neuronal interactions underlying the emergence of structured spontaneous activity. Remarkably, tectal assemblies are not necessarily driven by common retinal inputs (Figure 5) and might exclusively rely on tectal recurrent connectivity (Deco et al., 2011; Ringach, 2009), although we cannot exclude the involvement of other brain sources. We observed all-or-nothing-like synergistic facilitation between assembly neurons, suited for their efficient and robust coordinated recruitment (Figures 6A and 6B). Moreover, we found evidence for lateral competitive dynamics between visually evoked neuronal groups (Figures 6C–6E), suggesting that biased reciprocal inhibitions between neighboring assemblies may shape their compact topography. Therefore, we expect that under weak external drive, these tectal dynamic principles will spontaneously generate structured activation patterns out of noise. This scenario is analogous to the heuristic optimization algorithm simulated annealing, where random small fluctuations drive stochastic exploration of an "energy landscape" (the tectum's dynamic repertoire), revealing stable system states (the neuronal assemblies). These states would represent robust neuronal circuit modes that may be dynamically recruited during sensory-induced brain responses (Destexhe, 2011; MacLean et al., 2005; Ringach, 2009), avoiding less reliable intermediate states

(B) Top: topography examples of spontaneous assemblies with step-like non-linear dynamics (assembly neurons in yellow). Bottom: corresponding raw data (dots) and regression fits (black curves) of the activation probabilities of the assembly's neurons. Note the all-or-none-like nature of these curves, suggesting highly recurrent facilitatory cooperative dynamics.

(C) Percentage of responsive neurons (top) and the population average of the mean $\Delta F/F$ responses across trials (bottom; only responsive neurons) of individual-light-spot and simultaneous-light-spot stimulation, schematically indicated by a single and a pair of black dots, respectively. Gray lines, single experiments; red lines, average. In top panel, percentages are relative to the combined total of neurons responsive to the two light spots presented individually.

(D) Two examples of single-trial (rasters) and average (bar plots) tectal response patterns to individual light spots (top and middle panels; 10 trials; red and green for most rostral and most caudal light spots, respectively) and simultaneous stimulation with both light spots (bottom panel, 20 trials, yellow). Grayscale: $\Delta F/F$ amplitude in rasters. Only responsive neurons are shown. Respective color-coded topographies of neurons that preferentially responded to either the most rostral or most caudal light spot in individual light-spot stimulation (top) and of the average $\Delta F/F$ tectal response pattern to simultaneous-light-spot stimulation (bottom). Note how responses to simultaneous stimulation are dominated by the most rostral or the most caudal light-spot representation in examples 1 and 2, respectively.

(E) Visualization of the linear decomposition analysis of the two examples shown in (D). Decomposition weights of single-trial responses to individual (red dots, rostral; green dots, caudal) and simultaneous (yellow dots) light spots with respect to the two average single-spot templates (bar plots in D). Dashed line: equal (balanced) weights. Note how yellow dots overlap with red (top) and green (bottom) dots.

(F) Left to right, visualization of the decomposition analysis of pooled experiments according to four categories: bias competition for rostral neuronal group, bias competition for the caudal group, alternated bias across trials, and balanced responses (no bias of a given group). Top: decomposition weights, color code as in (E). Bottom: distributions of the corresponding imbalance indexes. As a control, we show the expected distribution for a balanced linear response summation scenario estimated from all the possible pair-wise sums of the corresponding individual-light-spot trial responses (black line).

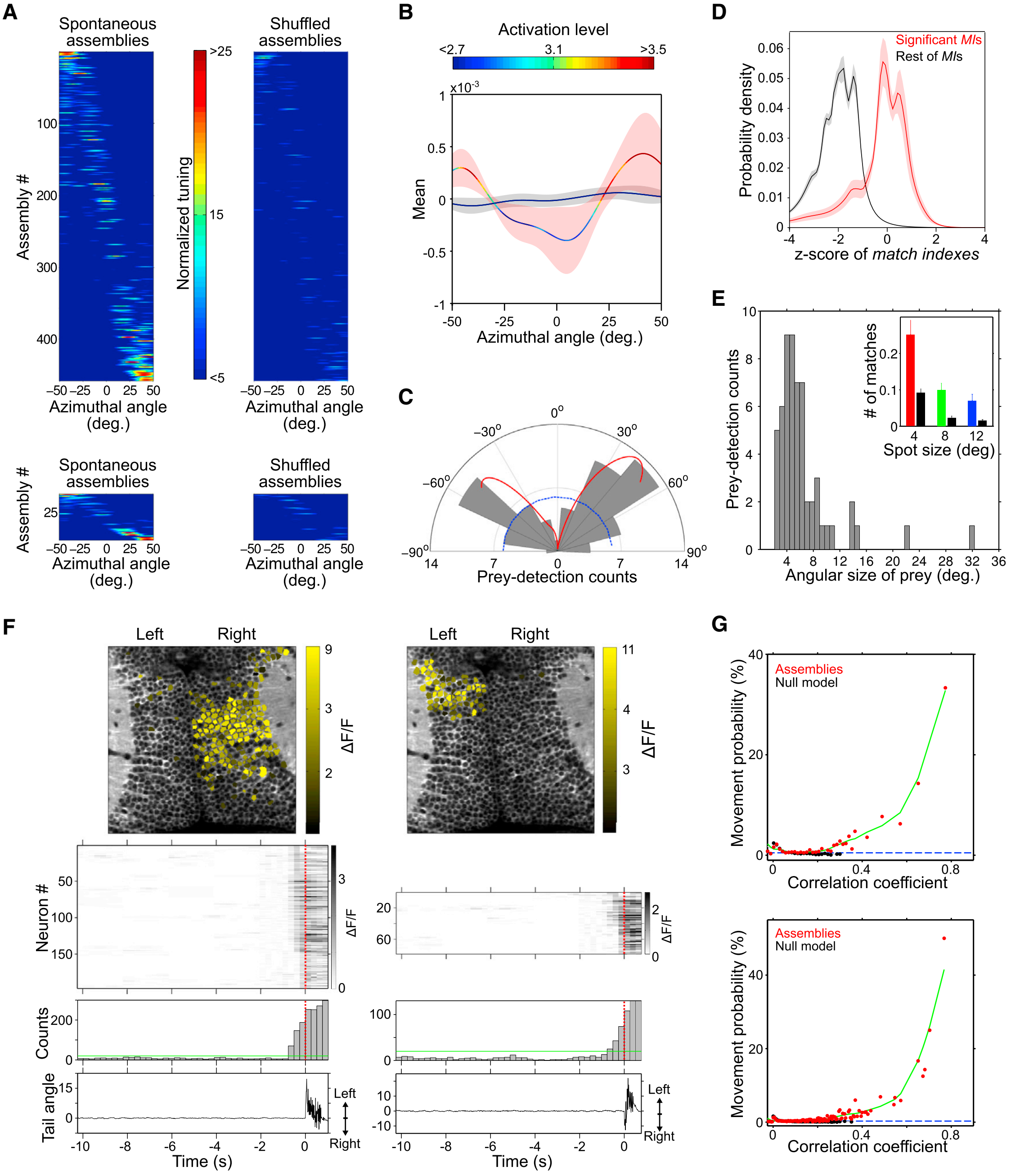

Figure 7. Behavioral Correlate of the Tectum's Spontaneous Neuronal Assemblies

(A) Normalized azimuthal tuning of all spontaneous assemblies from all experiments (top left, n = 9) and for a typical experiment (bottom left). Same analysis for the null model runs (right). Color scale bar, normalized azimuthal tuning.

(B) Average across experiments of the mean normalized azimuthal tuning of spontaneous assemblies (curve with red confidence interval) and the null model runs (curve with black confidence interval). Confidence intervals, SD. Curves are color-coded according to the average activation levels for each azimuth angle (top color bar). Note the clear over-representation of lateral positions in both spatial tuning and activation.

(C) Polar plot of the relative angle between the larva and the *paramecia* at the detection instant preceding a prey-capture behavior (gray bars, n = 60). Negative angles: right visual field. Blue dashed line indicates homogeneous angular performance. Red curve: mean normalized azimuthal tuning of spontaneous assemblies as in (B), positioned and rescaled to have the same mean and range as the gray bars to allow comparison. Note the similar trend between the behavioral and spontaneous activity preferences.

(D) Probability density distributions of the significant (red) and non-significant (black) MIs between spontaneous assembly patterns and the 4°-light-spot average response patterns, Z scored with respect to the MIs across the corresponding stimulation trials. Confidence intervals: jackknife procedure. 89% of the significant MIs between stimulated groups and spontaneous assemblies lay between Z score values of -2 and 2, suggesting match levels comparable to the ones obtained across trials of the concerned light-spot stimulations.

(legend continued on next page)

(Marre et al., 2009). This points to spontaneous assemblies as an unavoidable consequence of the optic tectum's functional role.

In the same line, spontaneous assemblies matched visual representations corresponding to angular sizes (4°) found to initiate a prey-capture behavior (Bianco et al., 2011; McElligott and O'malley, 2005) (Figures 7D and 7E). This could reflect the tectum's functional strategy for reducing the high dimensionality of the external world by the formation of tectal functional subnetworks, whose visual resolving capability is suited to extract information of vital importance to the organism. Indeed, the tectum is involved in behaviors that require the visual detection of small objects by means of an identified neuronal circuit capable of filtering large visual stimuli, making it most responsive to 4° stimuli (Del Bene et al., 2010). The filtered visual inputs would favor the tectal representation for angular sizes of 4° through experience-dependent plasticity, explaining their preponderance in spontaneous activity. In the same line, the population of spontaneous tectal assemblies showed an over-representation for lateral regions of the visual field (Figure 7B), which matched the observed behavioral tendency in visual detection performance (Figure 7C). These observations suggest that the structure of the tectal spontaneous activity showed features also observed at the behavioral level, stressing its biological significance. Furthermore, we showed that the activation of a spontaneous tectal assembly significantly increased the probability of a subsequent spontaneous tail movement (Figure 7G), demonstrating a behavioral correlate of patterned spontaneous activity in a sensory brain region. Spontaneous behaviors were preceded by compact tectal assemblies in only 11% of the cases. We thus interpret these events as a reflection of the tectal functional connectivity adapted for robust visual detection of biologically relevant features and the generation of orienting motor commands.

Neuronal clusters showing spontaneously correlated activity do not necessarily imply neuronal interconnectivity, but could reflect functional processing modules (Harris, 2005). Our results indicate that tectal spontaneous spatiotemporal activity patterns represent robust "preferred" network states compatible with tectal functional principles, adapted for robust visual detection, associated in some cases with orienting motor behaviors. This suggests that structured tectal spontaneous activity emerges from neuronal mechanisms suited for the tectum's role in vital behaviors such as prey tracking in low-contrast, crowded, cluttered natural environments.

Alternatively to this scenario, the compact neuronal assemblies could represent active top-down cognitive process (Engel et al., 2001; Ringach, 2009) (e.g., spatial attention or expectations), while the sparse ones may reflect global network modulations induced by the cholinergic or serotonergic systems.

EXPERIMENTAL PROCEDURES

Animals

Experiments were performed in 8 days post-fertilization (dpf) larvae of a transgenic *Huc:GCaMP3* Nacre line. All experiments were approved by *Le Comité d'Éthique pour l'Expérimentation Animale Charles Darwin* (Ce5/2009/027).

In Vivo Calcium Imaging

Larvae were restrained in 1.8% low-melting agarose and placed within a cylindrical chamber filled with E3 embryo medium (Figure 1A). Calcium dynamics were monitored using a custom-built two-photon microscope with a 25× NA1.05 objective and a Ti:sapphire laser tuned at 920 nm. Scanning was performed at 3.91 Hz on ~200 μm × 200 μm optic tectum planes at different depths. When simultaneously monitoring behavior, we filmed tail movements of head-restrained larva illuminated with an 820 nm LED, using a mini microscope connected to a high-speed camera (200 Hz) with a FF01-842 Semrock short-pass filter. For synchronization of video recordings, visual stimuli, and two-photon imaging, we used a I/O TTL board.

Visual Stimulation

Visual stimuli covered a field of view of ~90° × 90°. Light-bar stimuli were 4° wide and moved in the four cardinal directions at 45°/s. Light spots lasted for 1 s. They were presented at 19 different positions, from −45° to 45° in steps of 5°. We performed four trials for each stimulation, and the inter-trial time interval was 7 s. Stimulation order was randomized.

Analysis of Neuronal Visual Responses

For each stimulation, we averaged across trials the neuronal responses within a 2 s time window after the trial onsets and only considered neurons that responded in at least 50% of the trials. Neuronal spatial tuning curves were estimated by the normalized sum of 10°-wide Gaussian curves centered at the 4°-light-spot azimuthal positions. Neuronal direction selectivity was the difference of the average neuronal responses to bars moving in opposite cardinal directions, divided by their sum. The direction selectivity vector of each neuron was the vectorial sum of their up-down and left-right selectivities.

Detection of Neuronal Assemblies

The method and its benchmarking are explained in detail in the Supplemental Experimental Procedures. Briefly, we first reduced the dimensionality of the neuronal network activity using principal component analysis (PCA) by only keeping principal components (PCs) with significant eigenvalues (Peyrache et al., 2010). To determine the neuronal composition of the assemblies, we worked on a space of obliquely rotated components (Lopes-dos-Santos et al., 2011), which tended to group the PC loadings along non-perpendicular rotated PCs (rPCs). Neurons were assigned to a given assembly defined by a rPC if their loadings on that rPC exceeded a data-driven threshold value.

(E) Histogram of the angular size of the prey (*paramecia*) on the larva's retina at the moment of detection. Note the peak around ~4°–5°. Inset: the number of spontaneous assemblies that significantly matched (as measured by MI) neuronal groups induced by light spots of 4° (red), 8° (green), and 12° (blue) per stimulated neuronal group, per experiment. The number of significant matches to spontaneous assemblies' topographical null models are shown in black. Note the better match for 4° light spots with respect to the larger light spots.

(F) Two examples of spontaneous activation of a topographically compact tectal assembly before a spontaneous tail movement. Bottom to top: tail angle trace (zero, a straight tail; positive, left bends; negative, right bends), histogram of the spontaneously active tectal neurons (green line, threshold for significant population events; red dotted line, tail-flip onset), raster plot of spontaneous activations of tectal neurons active before the movement's onset (red dotted line, tail-flip onset), and topography of the spontaneously activated assembly. Time is relative to tail-flip onset. Note that neurons activated immediately before movement onset are located in the tectal hemisphere contralateral to the initial tail movement direction.

(G) Probability of a tail movement onset as a function of the correlation between all the assembly patterns and the spontaneous tectal network activity for the imaging frame preceding movement onset (red dots, raw data; green curve, regression fit). Black dots and curve: same calculation for randomized assemblies (null models). Dashed blue line: average probability of a movement onset at any given imaging frame. Top, typical experiment; bottom, pooled experiments (n = 5).

Matching Index

The MI quantifies the proportion of neuronal activations that are common to two given network activation patterns, with respect to the total number of activations present in both patterns. It is defined as

$$MI_{ij} = 2\frac{|Pat_i \cap Pat_j|}{|Pat_i| + |Pat_j|},$$

where both Pat_i and Pat_j are binary network activation patterns (binary vectors representing the imaged neuronal population, with ones indicating active neurons and zeros for the silent ones).

SUPPLEMENTAL INFORMATION

Supplemental Information includes Supplemental Experimental Procedures and seven figures and can be found with this article online at http://dx.doi.org/10.1016/j.neuron.2015.01.027.

AUTHOR CONTRIBUTIONS

S.A.R. carried out the imaging experiments, analyzed the data, and built the setup and software. T.P. generated the *elav3*:GCaMP3 transgenic line, participated in discussions about the data, and performed some eye enucleations. V.P.-S., A.J., and G.S. built the setup. M.H. carried out the behavioral assays. V.P.-S. and A.J. developed software. S.A.R. and G.S. conceived the experiments and wrote the manuscript.

ACKNOWLEDGMENTS

We thank M.-m. Poo, B. Barbour, Y. Frégnac, G. de Polavieja, and Y. Loewenstein for comments on the manuscript and E. Schenidman, J. Boulanger-Weill, and M.S. Murmu for helpful discussions. This work was supported by EraSysBio+ Zebrain, ERC stg 243106, ANR-10-LABX-54 MEMO LIFE, ANR-11-IDEX-0001-02 PSL* Research University, and Avenir grant INSERM.

Received: August 25, 2014
Revised: December 19, 2014
Accepted: January 22, 2015
Published: February 19, 2015

REFERENCES

Ahrens, M.B., Li, J.M., Orger, M.B., Robson, D.N., Schier, A.F., Engert, F., and Portugues, R. (2012). Brain-wide neuronal dynamics during motor adaptation in zebrafish. Nature *485*, 471–477.

Arieli, A., Sterkin, A., Grinvald, A., and Aertsen, A. (1996). Dynamics of ongoing activity: explanation of the large variability in evoked cortical responses. Science *273*, 1868–1871.

Azouz, R., and Gray, C.M. (1999). Cellular mechanisms contributing to response variability of cortical neurons in vivo. J. Neurosci. *19*, 2209–2223.

Berkes, P., Orbán, G., Lengyel, M., and Fiser, J. (2011). Spontaneous cortical activity reveals hallmarks of an optimal internal model of the environment. Science *331*, 83–87.

Bianco, I.H., Kampff, A.R., and Engert, F. (2011). Prey capture behavior evoked by simple visual stimuli in larval zebrafish. Front. Syst. Neurosci. *5*, 101.

Burrill, J.D., and Easter, S.S., Jr. (1994). Development of the retinofugal projections in the embryonic and larval zebrafish (Brachydanio rerio). J. Comp. Neurol. *346*, 583–600.

Carr, M.F., Jadhav, S.P., and Frank, L.M. (2011). Hippocampal replay in the awake state: a potential substrate for memory consolidation and retrieval. Nat. Neurosci. *14*, 147–153.

Deco, G., Jirsa, V.K., and McIntosh, A.R. (2011). Emerging concepts for the dynamical organization of resting-state activity in the brain. Nat. Rev. Neurosci. *12*, 43–56.

Deco, G., Jirsa, V.K., and McIntosh, A.R. (2013). Resting brains never rest: computational insights into potential cognitive architectures. Trends Neurosci. *36*, 268–274.

Del Bene, F., Wyart, C., Robles, E., Tran, A., Looger, L., Scott, E.K., Isacoff, E.Y., and Baier, H. (2010). Filtering of visual information in the tectum by an identified neural circuit. Science *330*, 669–673.

Destexhe, A. (2011). Intracellular and computational evidence for a dominant role of internal network activity in cortical computations. Curr. Opin. Neurobiol. *21*, 717–725.

Engel, A.K., Fries, P., and Singer, W. (2001). Dynamic predictions: oscillations and synchrony in top-down processing. Nat. Rev. Neurosci. *2*, 704–716.

Faisal, A.A., Selen, L.P.J., and Wolpert, D.M. (2008). Noise in the nervous system. Nat. Rev. Neurosci. *9*, 292–303.

Fiser, J., Chiu, C., and Weliky, M. (2004). Small modulation of ongoing cortical dynamics by sensory input during natural vision. Nature *431*, 573–578.

Fox, M.D., Snyder, A.Z., Vincent, J.L., Corbetta, M., Van Essen, D.C., and Raichle, M.E. (2005). The human brain is intrinsically organized into dynamic, anticorrelated functional networks. Proc. Natl. Acad. Sci. USA *102*, 9673–9678.

Gahtan, E., Tanger, P., and Baier, H. (2005). Visual prey capture in larval zebrafish is controlled by identified reticulospinal neurons downstream of the tectum. J. Neurosci. *25*, 9294–9303.

Gebhardt, C., Baier, H., and Del Bene, F. (2013). Direction selectivity in the visual system of the zebrafish larva. Front Neural Circuits *7*, 111.

Goldberg, J.A., Rokni, U., and Sompolinsky, H. (2004). Patterns of ongoing activity and the functional architecture of the primary visual cortex. Neuron *42*, 489–500.

Han, F., Caporale, N., and Dan, Y. (2008). Reverberation of recent visual experience in spontaneous cortical waves. Neuron *60*, 321–327.

Harris, K.D. (2005). Neural signatures of cell assembly organization. Nat. Rev. Neurosci. *6*, 399–407.

Harris, K.D., and Thiele, A. (2011). Cortical state and attention. Nat. Rev. Neurosci. *12*, 509–523.

Hilgetag, C., Kötter, R., Stephan, K., and Sporns, O. (2002). Computational methods for the analysis of brain connectivity. In Computational Neuroanatomy–Principles and Methods, G. Ascoli, ed. (Totowa: Humana Press), pp. 295–335.

Kenet, T., Bibitchkov, D., Tsodyks, M., Grinvald, A., and Arieli, A. (2003). Spontaneously emerging cortical representations of visual attributes. Nature *425*, 954–956.

Kerr, J.N.D., de Kock, C.P.J., Greenberg, D.S., Bruno, R.M., Sakmann, B., and Helmchen, F. (2007). Spatial organization of neuronal population responses in layer 2/3 of rat barrel cortex. J. Neurosci. *27*, 13316–13328.

Krauzlis, R.J., Lovejoy, L.P., and Zénon, A. (2013). Superior colliculus and visual spatial attention. Annu. Rev. Neurosci. *36*, 165–182.

Lopes-dos-Santos, V., Conde-Ocazionez, S., Nicolelis, M.A.L., Ribeiro, S.T., and Tort, A.B.L. (2011). Neuronal assembly detection and cell membership specification by principal component analysis. PLoS ONE *6*, e20996.

Luczak, A., Barthó, P., and Harris, K.D. (2009). Spontaneous events outline the realm of possible sensory responses in neocortical populations. Neuron *62*, 413–425.

Luczak, A., Bartho, P., and Harris, K.D. (2013). Gating of sensory input by spontaneous cortical activity. J. Neurosci. *33*, 1684–1695.

MacLean, J.N., Watson, B.O., Aaron, G.B., and Yuste, R. (2005). Internal dynamics determine the cortical response to thalamic stimulation. Neuron *48*, 811–823.

Marre, O., Yger, P., Davison, A.P., and Frégnac, Y. (2009). Reliable recall of spontaneous activity patterns in cortical networks. J. Neurosci. *29*, 14596–14606.

McElligott, M.B., and O'malley, D.M. (2005). Prey tracking by larval zebrafish: axial kinematics and visual control. Brain Behav. Evol. *66*, 177–196.

Mohajerani, M.H., Chan, A.W., Mohsenvand, M., LeDue, J., Liu, R., McVea, D.A., Boyd, J.D., Wang, Y.T., Reimers, M., and Murphy, T.H. (2013). Spontaneous cortical activity alternates between motifs defined by regional axonal projections. Nat. Neurosci. *16*, 1426–1435.

Niell, C.M., and Smith, S.J. (2005). Functional imaging reveals rapid development of visual response properties in the zebrafish tectum. Neuron *45*, 941–951.

Orger, M.B., Kampff, A.R., Severi, K.E., Bollmann, J.H., and Engert, F. (2008). Control of visually guided behavior by distinct populations of spinal projection neurons. Nat. Neurosci. *11*, 327–333.

Petersen, C.C.H., Hahn, T.T.G., Mehta, M., Grinvald, A., and Sakmann, B. (2003). Interaction of sensory responses with spontaneous depolarization in layer 2/3 barrel cortex. Proc. Natl. Acad. Sci. USA *100*, 13638–13643.

Peyrache, A., Benchenane, K., Khamassi, M., Wiener, S.I., and Battaglia, F.P. (2010). Principal component analysis of ensemble recordings reveals cell assemblies at high temporal resolution. J. Comput. Neurosci. *29*, 309–325.

Raichle, M.E., MacLeod, A.M., Snyder, A.Z., Powers, W.J., Gusnard, D.A., and Shulman, G.L. (2001). A default mode of brain function. Proc. Natl. Acad. Sci. USA *98*, 676–682.

Ringach, D.L. (2009). Spontaneous and driven cortical activity: implications for computation. Curr. Opin. Neurobiol. *19*, 439–444.

Shadlen, M.N., and Newsome, W.T. (1998). The variable discharge of cortical neurons: implications for connectivity, computation, and information coding. J. Neurosci. *18*, 3870–3896.

Smith, M.A., and Kohn, A. (2008). Spatial and temporal scales of neuronal correlation in primary visual cortex. J. Neurosci. *28*, 12591–12603.

Sumbre, G., Muto, A., Baier, H., and Poo, M.M. (2008). Entrained rhythmic activities of neuronal ensembles as perceptual memory of time interval. Nature *456*, 102–106.

Tian, L., Hires, S.A., Mao, T., Huber, D., Chiappe, M.E., Chalasani, S.H., Petreanu, L., Akerboom, J., McKinney, S.A., Schreiter, E.R., et al. (2009). Imaging neural activity in worms, flies and mice with improved GCaMP calcium indicators. Nat. Methods *6*, 875–881.

Tomasi, D., Wang, G.J., and Volkow, N.D. (2013). Energetic cost of brain functional connectivity. Proc. Natl. Acad. Sci. USA *110*, 13642–13647.

Treisman, M. (1964). Noise and Weber's law: the discrimination of brightness and other dimensions. Psychol. Rev. *71*, 314–330.

Tsodyks, M., Kenet, T., Grinvald, A., and Arieli, A. (1999). Linking spontaneous activity of single cortical neurons and the underlying functional architecture. Science *286*, 1943–1946.

Neuron, Volume *85*

Supplemental Information

Spontaneous Neuronal Network Dynamics Reveal Circuit’s Functional Adaptations for Behavior

Sebastián A. Romano, Thomas Pietri, Verónica Pérez-Schuster, Adrien Jouary, Mathieu Haudrechy, and
Germán Sumbre

Supplementary Figures

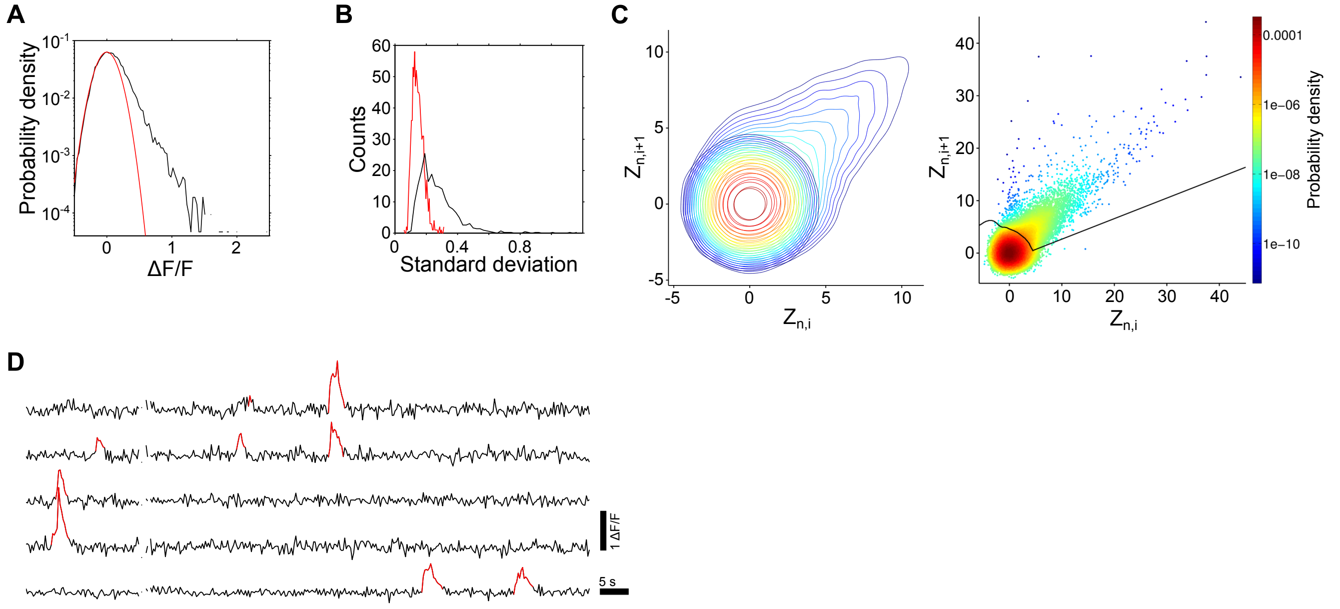

Figure S1, related to Experimental Procedures. Detection of GCaMP3 fluorescence events associated with calcium transients. (A) Probability density of relative change in fluorescence (ΔF/F) of a typical neuron (black) and the corresponding Gaussian fit to its negative ΔF/F values (red), used to estimate the standard deviation (s.d.) of the ΔF/F baseline, *B*. (B) Histogram of the ΔF/F s.d. (black) and the estimated σ_{noise} of one experiment. (C) Left, color-coded contour plots of the probability densities of the $Z_{n,i} \rightarrow Z_{n,i+1}$ transitions observed in an experiment (positively skewed contour plot) and for the baseline *B* model (round-shaped contour plot) are overlaid for comparison. The distributions were smoothly estimated by a bivariate locally adaptive density estimation procedure. Right, scatter plot of the $Z_{n,i} \rightarrow Z_{n,i+1}$ transitions, color-coded according to their probability densities. The range of transitions that were inferred as part of a neuronal calcium transient is outlined by the black curve ($p < 0.05$). This boundary is composed by a straight line that corresponds to the constraint imposed by GCaMP3 decay time constant, and a curved perimeter that is given by the noise model *B*. Color bar, probability density values. See Supplementary Experimental Procedures for details. (D) Examples of typical single-neuron ΔF/F traces (black) with significant fluorescence transients highlighted in red. Breaks in the traces depict discarded frames due to movement artifacts.

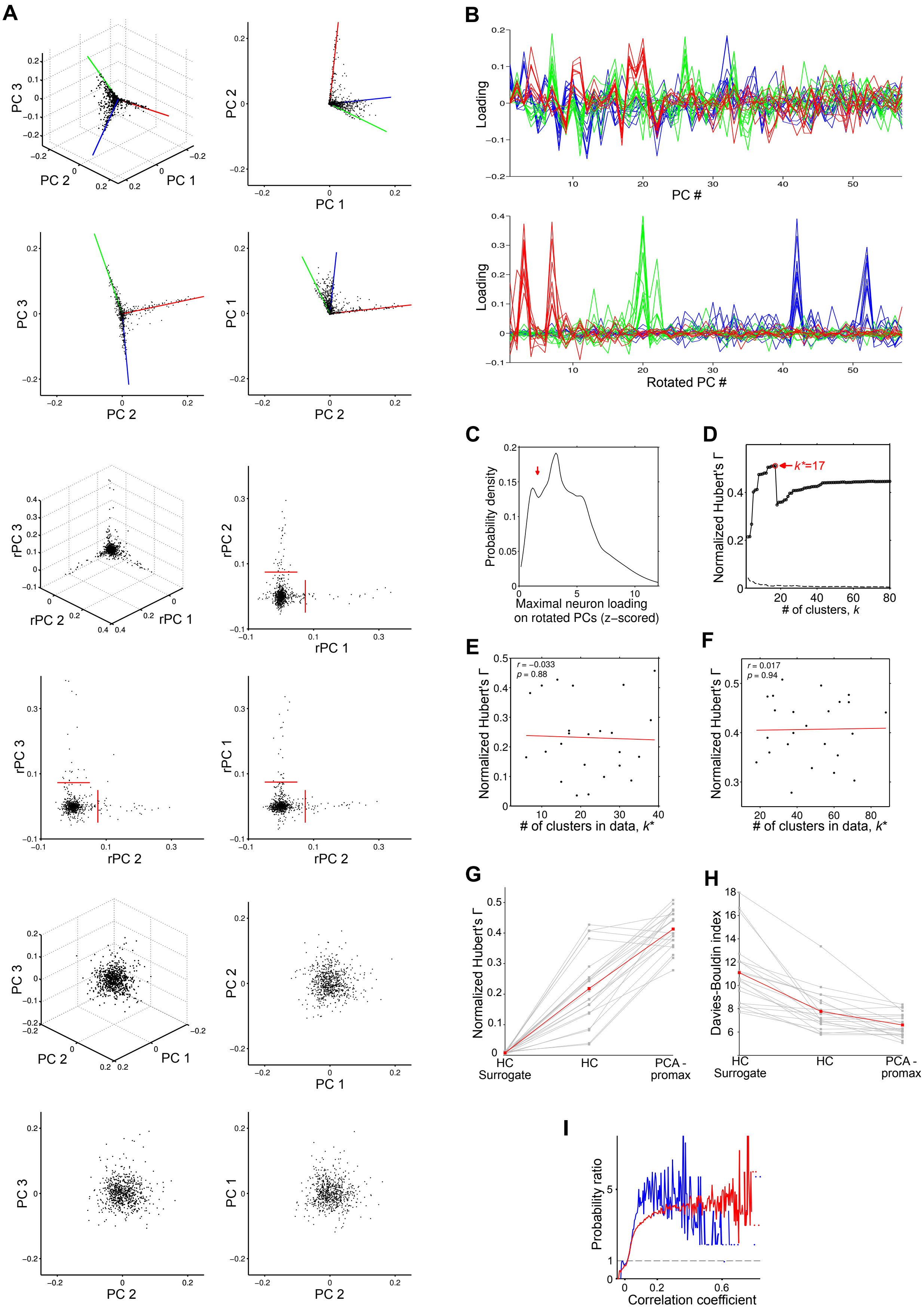

Figure S2, related to Figure 4. Neuronal assemblies' detection method. (A) Examples of neuronal population activity observed in principal component (PC) space. Only the first 3 most significant PCs are shown (see B for a representation of all the significant PCs). Each black dot depicts a neuron, its coordinates are given by the entire neurons' spontaneous activity during 1hr recordings. A typical experiment is shown in the 4 upper panels. Notice the dots extending along straight lines projecting away from the origin. This is not observed for *IAI* shuffled data (4 bottom panels). The axes that describe these projections are obtained by *promax* rotation of the PCs (red, green and blue lines). The data is represented over these rotated PCs (rPCs, 4 middle panels), and a threshold (red lines, see c) delineates the assemblies. (B) The component loadings of neurons from 3 assemblies (red, green and blue curves) over all the significant PCs (top) and rPCs (bottom). Each curve depicts a neuron, representing all its loadings over the corresponding component axes. Note the overlap between similar color curves, indicating that neurons with similar loadings in the rPC space belong to the same assembly. (C) Probability density of the maximal neuronal loadings on rPCs, z-scored with respect to all the loadings of the concerned rPC, of a representative experiment. These distributions typically show a first peak that encompasses the cloud of points scattered around the origin of the rPC space (see middle panels of A). The threshold for rPC loadings that discriminated assemblies (red lines in the middle panels of A) was manually selected from this distribution (red arrow). Its value was usually around 2, and small variations in its definition did not affect the validity of the assemblies, as measured through clustering validation techniques. (D) Example of the normalized Hubert's Γ as a function of the number of clusters, *k*, used for *hierarchical clustering* of the matrix *D* of a spontaneous activity dataset previously projected in the significant PC space (solid line). The control corresponding to the average of 1000 randomized surrogate datasets of neuronal activity is shown in dashed line. The final number of clusters chosen for the clustering procedure, *k**, corresponds to the value that maximizes Γ (red circle, *k**=17). (E, F) The normalized Hubert's Γ as a function of *k**, for hierarchical clustering (left) and the combined *PCA-promax* procedure (right). Dots are different experiments, red lines show linear regressions. *r*, correlation coefficient; *p*, *p*-value. (G) Comparison of the clustering performances, as measured by Γ, for *hierarchical clustering* (HC) of spontaneous activity datasets and the *PCA-promax* of spontaneous activity datasets. As a reference, we also show the result for HC of the surrogate datasets. Single experiments are shown in gray, average across experiments in red. (H) Same as G, but for the Davies-Bouldin index. (I) The *PCA-promax* to HC ratio of the probability of including a neuronal pair in a cluster as a function of their spontaneous activity correlation coefficient, for all the experiments pooled (red) and for a representative experiment (blue). Equal performance (ratio=1) is marked by dashed line. Notice how PCA-promax tends to include ~5-fold more positive correlations than HC.

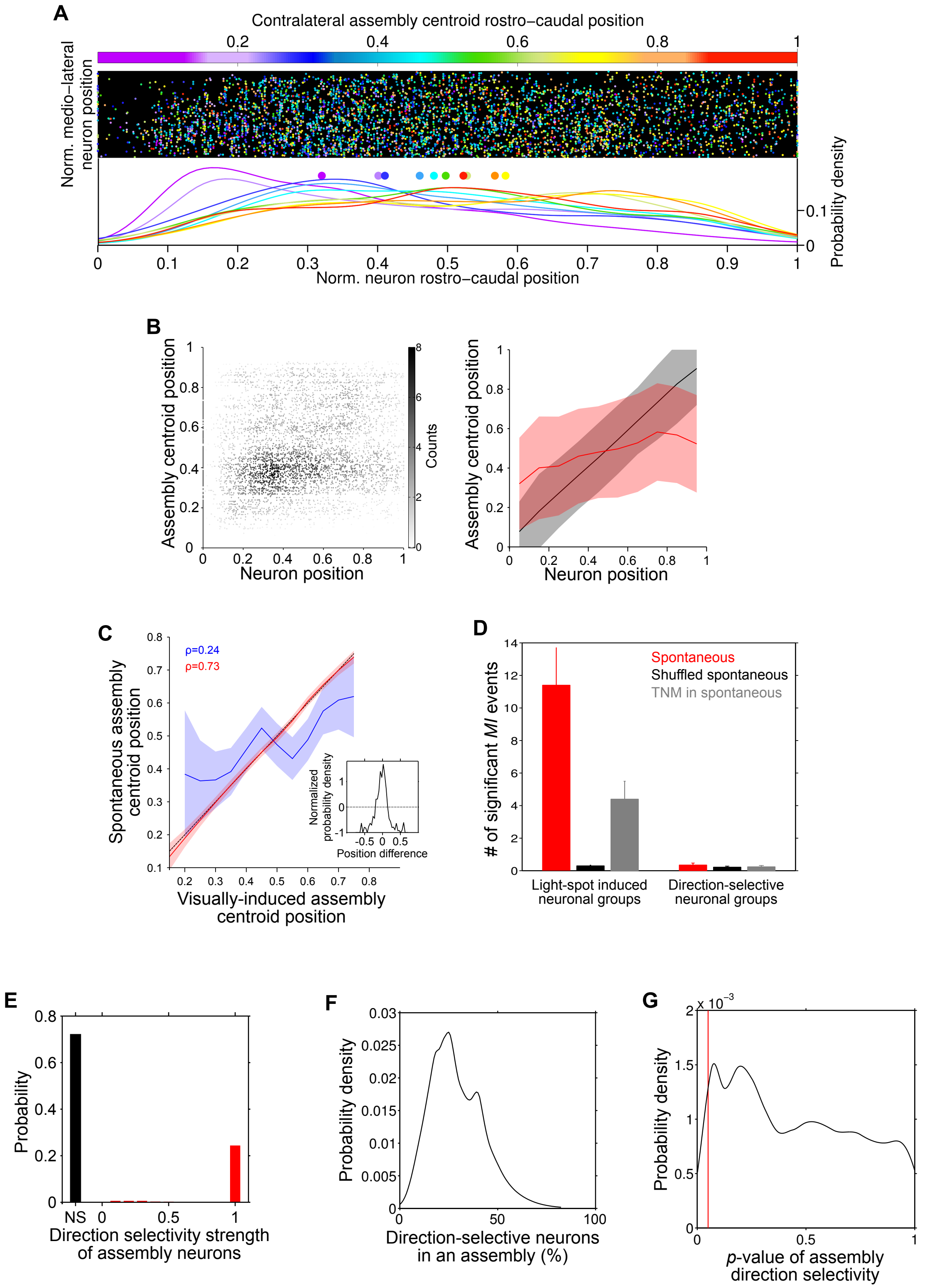

Figure S3, related to Figure 3 and 4. Spontaneous assemblies resemble visual representations, are not topographically organized across tectal hemispheres and do not represent the direction-selective organization. (A) Normalized topography of spontaneous assemblies across larvae (n=23), considering only assemblies whose centroids lie in the opposite tectal hemisphere to the represented neuron. Top, each point represents the normalized position of a neuron participating in a spontaneous assembly, whose color indicates the normalized rostro-caudal centroid positions of its assemblies (color bar on top). Bottom, probability density distributions of the normalized rostro-caudal position of neurons for assemblies within the same range of colors (for 10 bins of the color bar). Colored dots, the medians for each distribution curve. (B) Left, density plot of the normalized rostro-caudal position of each neuron against the normalized rostro-caudal centroid position of its spontaneous assemblies laying on the opposite tectal hemisphere. Grey scale, data count. Right, local regression to the data (red). For comparison, we superimposed the result for the assemblies in the same hemisphere (black, local regression of data in **Figure 4E**). Note the low correlation for assemblies with centroids in the contralateral tectum ($r = 0.14$, $p < 10^{-5}$, with only 2% of the variance explained by the linear fit with a slope of 0.12) with respect to assemblies with centroids within the same tectum ($r = 0.7$, $p < 10^{-5}$, with 49% of the variance explained by the linear fit with a slope of 0.61), suggesting that no clear topographic organization was observed across tectal hemispheres. Confidence intervals, s.d. (C) The correlation between the normalized centroids of visually induced (VI) and spontaneous assemblies, belonging to the same (red) and opposite (blue) hemispheres (n=9). Lines and confidence intervals, local regression fit and 95% confidence interval of fit. Pearson's correlations r=0.73, $p<10^{-5}$; r=0.24, p=0.002. The dashed black line represents a 1 to 1 relationship. Note that for a given neuron participating in spontaneous and VI assemblies on the same tectal hemisphere, the normalized rostro-caudal centroid position of its VI assemblies linearly predicts those of its spontaneous assemblies (red line), suggesting that the spontaneous dynamics follow a retinotopic-like organization. In contrast, spontaneous assembly centroids within the opposite hemisphere showed no correlation (blue line). Inset, the probability density distribution of the differences between the normalized centroid positions of spontaneous and VI assemblies from the same hemisphere. The distribution was normalized with respect to the average null model, with positive density values indicating an over-representation. Note that the majority of the observed assemblies show similar spontaneous and VI normalized centroid positions. (D) Same as **Figure 4F**, also showing the average number of significant *MI* events, during spontaneous activities, of *topographical null models* of visually evoked neuronal groups (gray), for light-spot stimulated (left) and direction-selective (right) neuronal groups. (E) Probability histogram of direction-selectivity strength (norm of direction preference vectors) of neurons in spontaneous assemblies. NS, non-selective. (F) Probability density distribution of the proportion of direction-selective neurons in spontaneous assemblies. (G) Probability density distribution of the significance of spontaneous assemblies direction-selectivity tunings (Supplementary Experimental Procedures). The red line sets the threshold of significance ($p = 0.05$). Only 4.8 % of the assemblies lay below this threshold, therefore we conclude that spontaneous assemblies are not particularly tuned to specific directions.

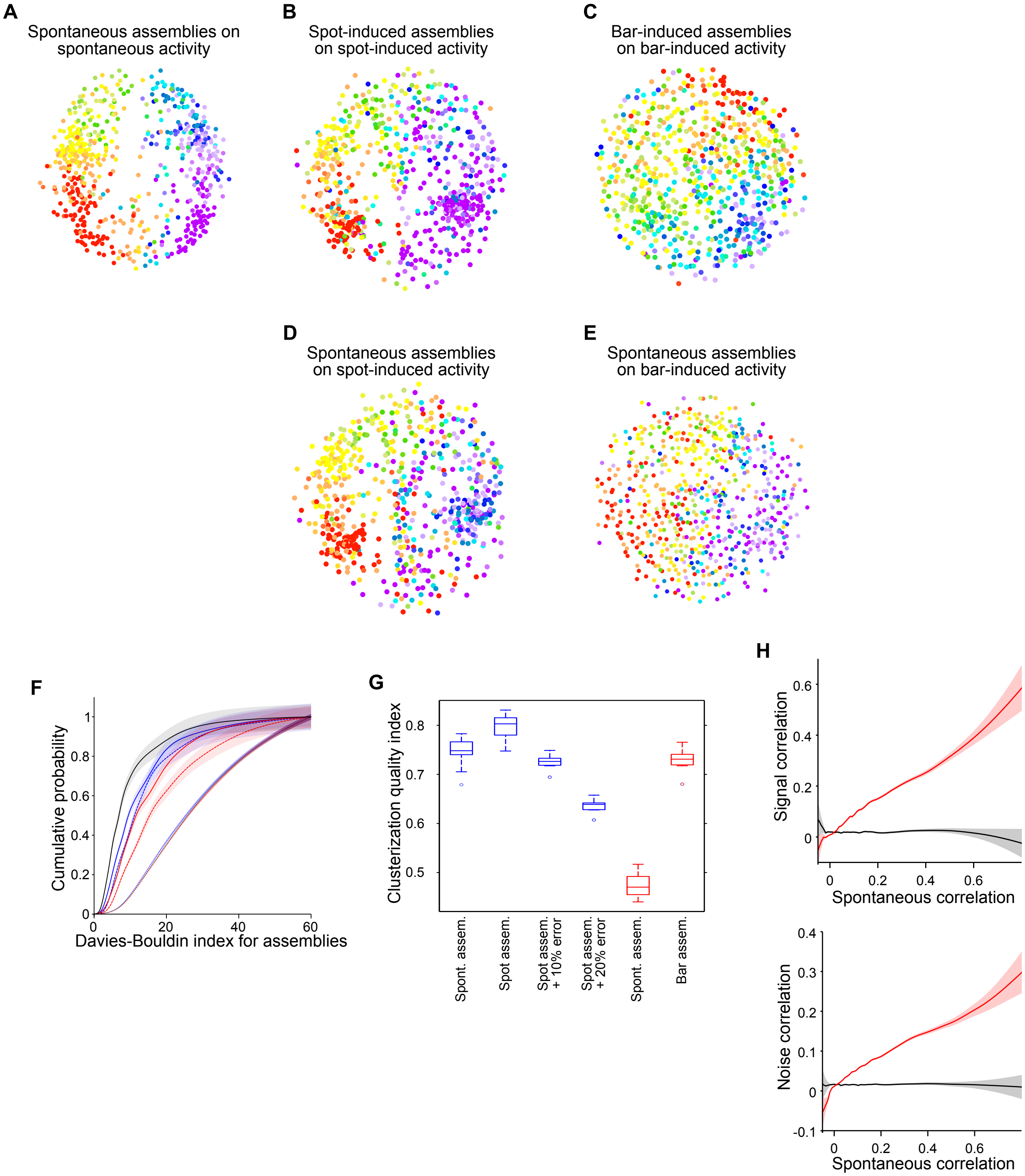

Figure S4, related to Figures 1,2 and 4. Relationship between spontaneous assemblies and visually induced activities (A-E) Validation of the spontaneous emergence of a functional retinotopic map by a *PCA-promax* independent technique, Multi-dimensional scaling (MDS). This technique produced bi-dimensional scatter plots, where points depict neurons, with the distances between points inversely proportional to the neuronal pair-wise correlations. MDS visualization of the neuronal population dynamics global structure in one typical experiment. Dots (neurons) are colored according to the indicated assembly partitionings, obtained through our algorithm for assembly detection (*PCA-promax*, independent to MDS). (A) Spontaneous activity colored according spontaneous assemblies.

Colors reasonably discriminate separated clusters, supporting the spontaneous assemblies found by *PCA-promax*. (B) Light-spot-stimulated activities colored according to light-spot-induced assemblies. (C) Moving-bar-stimulated activities colored according to moving-bar-induced assemblies. (D) Light-spot-stimulated activities colored according to spontaneous assemblies. The resemblance to B suggests that spontaneous assemblies satisfactorily explain the structure of light-spot-stimulated activities. (E) Moving-bar-stimulated activities colored according to spontaneous assemblies. (F) Cumulative probability densities of the Davies-Bouldin (DB) index for assemblies, which quantifies the validity of the assemblies. A particular partitioning is of a better quality if its cumulative distribution peaks sooner and steeper. We present the DB index distributions for spontaneous activities clustered according to the spontaneous assemblies (solid black line, A), light-spot-induced activities clustered according to light-spot-induced assemblies (solid red line, C). We also present the distributions for spontaneous assemblies clustering light-spot-induced activity (dashed blue line, D) and moving-bar-induced activities (dashed red line, E), and the null models of assemblies clustering light-spot-induced activities (dotted blue line) and moving-bar-induced activities (dotted red line). All experiments were pooled and error bars are calculated by jackknife procedure. (G) Box-plot of the *clustering quality index* (see Supplemental Experimental Procedures) of light-spot-induced activity (blue) and moving-bar-induced activity (red) data. Assemblies used for the light-spot-induced activity are (from left to right, see labels on abscissa) spontaneous assemblies, light-spot-induced assemblies, light-spot-induced assemblies + 10 % error, light-spot-induced assemblies + 20 % error. For moving-bar-induced activity, we used spontaneous assemblies and moving-bar-induced assemblies. The partitioning given by spontaneous assemblies explains the structure of light-spot-induced activity as good as the partitioning given by light-spot-induced assemblies + 10 % error ($p > 0.05$). (H) Relationship between signal (top) and noise (bottom) pair-wise correlations with the spontaneous pair-wise correlations. Red, data. Black, same analysis after randomizing the neuronal pair ordering of the respective signal and noise correlations. Curves, local regressions. Patches, confidence intervals. Signal and noise correlations were calculated with neuronal responses to light-spot stimulations (n=9).

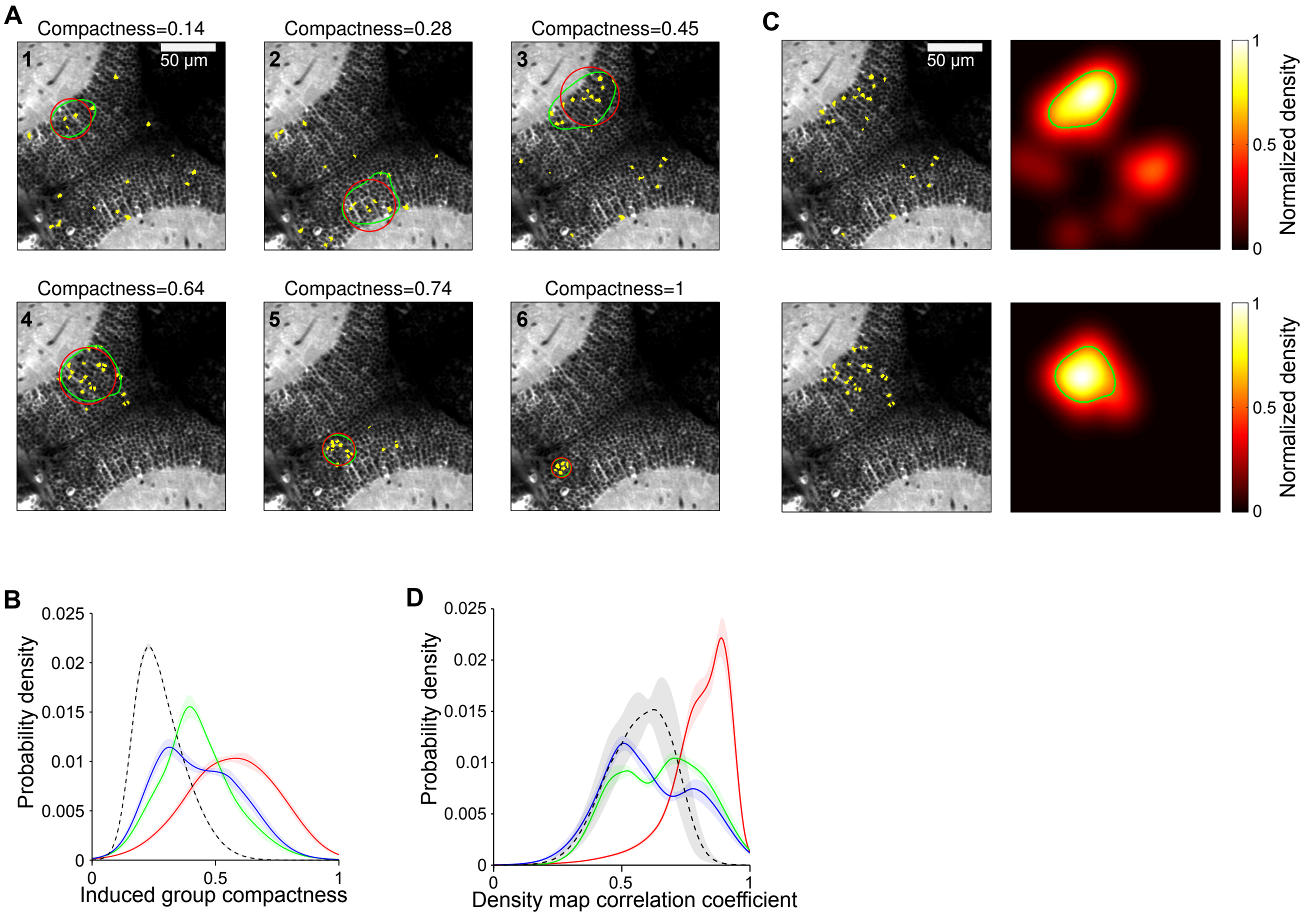

Figure S5, related to Figure 7. Spontaneous assemblies' activation patterns better match those of compact neuronal groups induced by small light spots. (A) Examples of the implementation of the algorithm used to calculate the *compactness index*, for 6 representative spontaneous assemblies of different *compactness index*. After calculation of smooth topography density maps (see C), we estimated the focal region occupied by the group of neurons (green contour) and we calculated the proportion of assembly neurons that resided inside a circle (red line) of an area equal to the area of the region occupied by the assembly, centered at the peak assembly density map. Notice how the index is proportional to the assemblies' topographical packing. (B) Probability density distributions of *compactness indexes* for neuronal groups activated by stimulating with light spots of 4° (red), 8° (green) and 12° (blue). The black dashed line is the compactness index distribution for null models. Confidence interval calculated by jackknife procedure. Note that the visually induced neuronal groups are significantly more compact that the null model. Light-spots of smaller angular sizes induced more compact neuronal groups (*compactness indexes* of higher values). (C) Examples of two spontaneous assemblies (left; assemblies 3 and 4 in A) and their topography density maps (right) with the focal regions they occupy delineated in green. Color bar, maximum-normalized topography density. (D) Probability density distributions of the correlation coefficient between topographical density maps of visually induced neuronal groups and their best-matching spontaneous assemblies, for light-spot stimulation of 4° (red), 8° (green) and 12° (blue). The black-dashed line is the probability density for null models. Confidence intervals calculated by jackknife procedure. The activation density map of neuronal groups stimulated by 4° light spots and those of spontaneous assemblies are significantly similar ($p < 10^{-5}$).

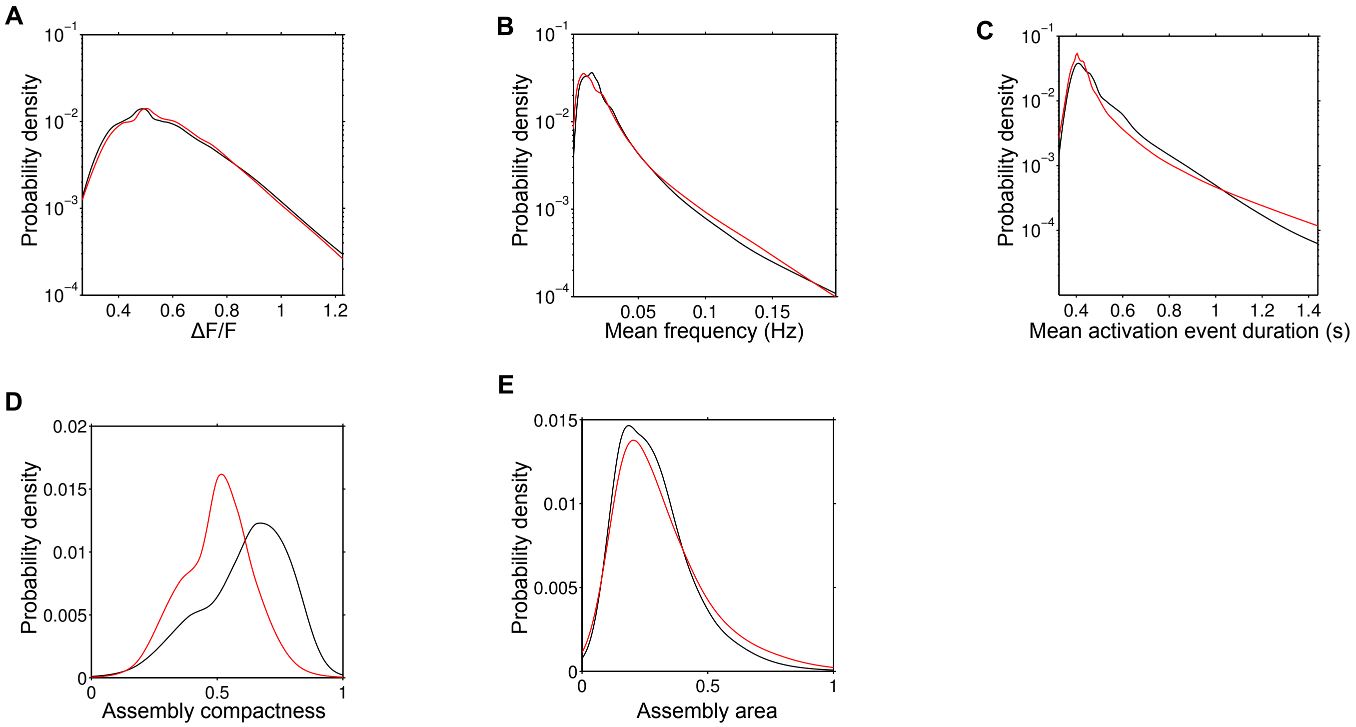

Figure S6, related to Figure 5. Retinal-input deprived neurons remain active as normal tecti, but they organize into less compact assemblies. (A-E) For the normal (black) and retinal-input deprived (red) tecti, the probability density distributions of significant neuronal DF/F events (A; $p > 0.05$), mean neuronal activation frequencies (B; $p = 0.005$), mean neuronal activation durations (C; $p < 10^{-5}$), spontaneous assembly compactness indexes (D; $p < 10^{-5}$), and spontaneous assembly areas (E; $p > 0.05$).

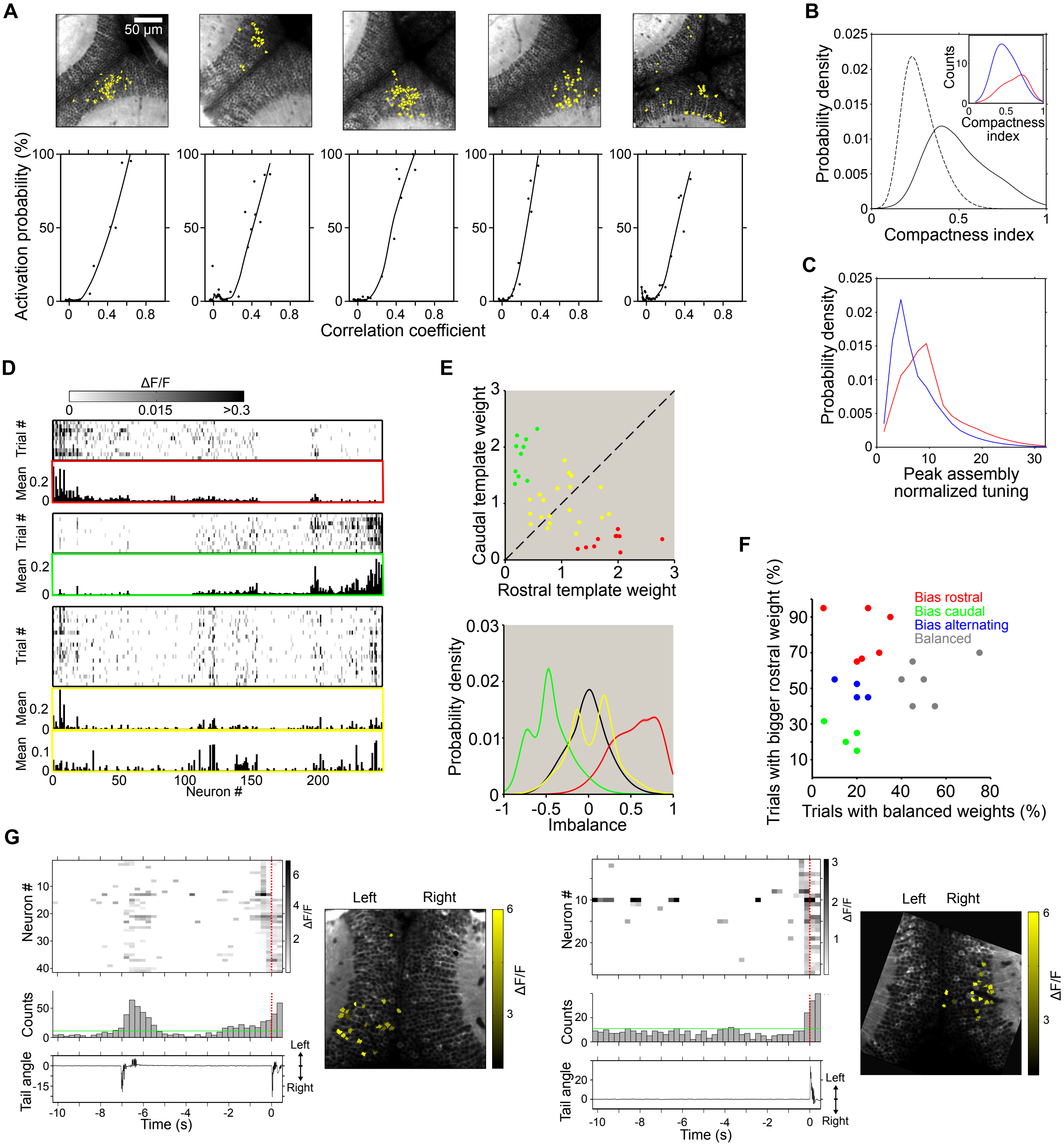

Figure S7, related to Figures 6-7. Tectal cooperative and competitive dynamics (A) Top, topography examples of spontaneous assemblies with step-like non-linear dynamics (assembly neurons in yellow). Bottom, corresponding raw data (dots) and regression fits (black curves) of the assembly neurons activation probabilities (see **Figure 6B** for more examples). (B) Probability density distribution of *compactness indexes* for spontaneous assemblies (solid line) and null models (dashed line). *Compactness index* of 0.54 ± 0.18 for spontaneous assemblies and 0.28 ± 0.1 for null models, mean and s.d., $p < 10^{-5}$. Inset, histograms of *compactness indexes* for spontaneous assemblies with linear (blue) and step-like non-linear (red) facilitations of neuronal activation probabilities. Note how step-like assemblies are more topographically compact that the linear ones. (C) Probability density distribution of the assembly normalized spatial-tuning curve peaks for linear (blue) and step-like non-linear (red) assemblies. Note that step-like assemblies tend to have a stronger spatial tuning with respect to azimuthal angular representations (p = 10^{-5}). (D)

Example of an experiment where domination in simultaneous-light-spot stimulation alternated across trials between the most rostral and most caudal neuronal groups. Single-trial (rasters) and average (bar plots) tectal response patterns to individual light-spots (top and middle panels; 10 trials; red and green for most rostral and most caudal light-spots, respectively) and simultaneous stimulation with both light-spots (bottom panel, 20 trials, yellow). For simultaneous-light-stimulation, trials in raster plots are ordered according to the dominating neuronal group (trials with rostral or caudal domination on the top and bottom half, respectively) and we present two bar plots, corresponding to the average tectal response patterns to the 10 uppermost trials (top, where rostral group dominates) and the remaining 10 lowermost trials (bottom, where caudal group dominates). Grey scale, DF/F amplitude in rasters. Only responsive neurons are shown. (E) Top, visualization of the linear decomposition analysis of example shown in D. Decomposition weights of single-trial responses to individual (red dots: rostral; green dots: caudal) and simultaneous (yellow dots) light-spots with respect to the two average single-spot templates (red and green bar plots in D). Dashed line, equal (balanced) weights. Bottom, distributions of the corresponding *imbalance indexes* of the decomposition shown on top. As a control we show the expected distribution for a balanced linear response summation scenario, estimated from all the possible pair-wise sums of the corresponding individual-light-spot trial responses (black line). (F) Analysis for pooling experiments where either the rostral (red) or the caudal (green) neuronal group dominates, where domination alternates between both groups (blue) and where both groups sum are represented in a balanced manner (gray). We considered a trial as having balanced decomposition if the corresponding weights in the weight pair were equal ±10%. (G) Two examples of spontaneous activations of a topographically compact tectal assemblies before spontaneous tail movements. Bottom to top, tail angle trace (zero: a straight tail, positive: left bends, negative: right bends), histogram of the spontaneously active tectal neurons (green line, threshold for significant population events; dotted-red line, tail-flip onset), raster plot of spontaneous activations of tectal neurons active before the onset of the tail movement (dotted red line: tail-flip onset). Time is relative to tail-flip onset. For each example, the topography of the spontaneously activated assembly is shown on the right. Note neurons activated immediately before movement onset are located in the tectal hemisphere contralateral to the initial tail movement direction.

SUPPLEMENTAL EXPERIMENTAL PROCEDURES

Zebrafish preparation

Experiments were performed in 8 dpf larvae of a transgenic *Huc:GCaMP3* nacre line that we generated as previously described (Panier et al., 2013). The *tol2 HuC:GCaMP3* vector was built by successive ligations of a 3.2 kb fragment of the zebrafish *HuC* (*elav3*) promoter (Park et al., 2000) (gift from HC Park, Kyungpook National University, Korea), then *GCaMP3* calcium probe (Tian et al., 2009) (gift from L. Looger, Howard Hughes Medical Institute, Ashburn, Virginia, USA) into pT2KXIG in (from K. Kawakami, National Institute of Genetics, Shizuoka, Japan). *HuC* promoter drives the expression of a RNA-binding protein and has been involved in neuronal differentiation. In zebrafish, the 3.2 kb proximal region encompassing 2771 base pairs of the 5′-upstream sequence up to the translation start site in +383/+385, has been shown to be sufficient to target specifically and efficiently all differentiated neurons (Park et al., 2000).

One cell stage Nacre zebrafish embryos (Lister et al., 1999) (*mitfa−/−*) were injected with 20 ng of the plasmid DNA and 25 ng of transposase RNA (generated from pCS-TP plasmid, K. Kawakami). Injected embryos were raised to adulthood and crossed individually with nacre fish to obtain F1 embryos. These embryos were then screened and selected according to their level of transgene expression. The embryos with the strongest expression were raised to adulthood and incrossed to obtain the homozygous *HuC:GCaMP3*^{GS5} line. The *HuC:GCaMP3*^{GS5} embryos were collected and raised at 28.5 °C in E3 embryo medium. Larvae were kept under 14/10 h on/off light cycles and fed after 6 dpf. All experiments were approved by *Le Comité d'Éthique pour l'Expérimentation Animale Charles Darwin* (Ce5/2009/027).

Two-photon calcium imaging

The imaging set-up was based on a MOM system (Sutter) with a 25x NA1.05 Olympus objective and a Mai Tai DeepSee Ti:sapphire laser tuned at 920 nm. The output power at the focal plane was less than 3 mW. The filters consisted of a FF705 dichroic (objective dichroic), a AFF01-680 short path (IR Blocker) and a FF01 520/70 band-pass filter, all from Semrock. The PMT was a H1070 (GaAsP) from Hamamatsu. The emission signal was pre-amplified with a SR-570 (Stanford Research Systems) and acquired using ScanImage (Pologruto et al., 2003) at 3.91 Hz, with 256 x 256 pixels resolution.

Larvae were embedded in 1.8 % low-melting agarose (Invitrogen) in E3 embryo medium (Westerfield, 2007) (in mM): 5 NaCl, 0.17 KCl, 0.33 CaCl2, 0.33 MgCl2 (pH 7.2); on an elevated stage within a cylindrical chamber filled with E3 embryo medium (**Figure 1A**). The optic tectum region was imaged at different planes, starting at ~30 µm bellow its surface and up to ~100 µm deep. Only those planes showing retinotopically organized visual responses were considered as tectal sensory visual regions, and were selected for further analysis. Planes showing no retinotopicity were discarded. Larvae were left to rest and adapt to the dark for at least 30 min before starting the experiments. We performed 23 experiments of ongoing spontaneous activities' from 15 larvae. On 9 of these experiments we also performed visual stimulation (7 larvae).

Due to the Ca^{2+} affinity of GCaMP3 (~400-660 nM, depending on the experimental conditions

(Akerboom et al., 2012; Tian et al., 2009)), neuronal activations involving less than a few spikes they were probably not detected by two-photon fluorescence imaging.

Visual stimulation

Visual stimuli were projected on a screen (#216 White Diffusion, Rosco Cinegel) around the recording chamber, using a pico-projector (refresh rate: 60 Hz., ADPP-305, Adapt mobile), covering a field of view of ~90º x 90º (azimuth x height). To avoid contamination of the fluorescence signal, we installed a 561 nm long-pass filter (BLP01-561R, Semrock) at the projector output lens that filtered green light. Larvae were carefully aligned to the projector with the help of a custom-made program that mapped azimuth angles on the chamber's projection screen.

Simulation consisted of moving light bars and fixed light spots. In order to minimize projection distortions due to the cylindrical chamber, we calibrated the projection to compensate as best as possible for the chamber's curvature. To confirm the stability of neuronal responses, we divided the stimulation protocol in 2 blocks (before and after the ongoing spontaneous activity recordings), each one consisting of 2 trials of all the stimulation set. Each set consisted of 4 bars moving in the four cardinal directions, and 19 light spots, each given at a specific azimuthal angles of the visual field. Overall, a total of 16 moving bars (4 per cardinal direction) and 76 light spots (4 per azimuthal angle) were presented per experiment. We discarded imaged videos without responses on either block. Bars were 4º-wide moving in the 4 cardinal directions at 45º per second. A single moving bar was presented per trial, covering the whole projected field of view. All light spots were presented at the same azimuthal plane, and had an angular size of 4º, 8º, or 12º. The light spots lasted for 1 second and were presented from -45º to 45º in steps of 5º (19 spots). The height (vertical plane) of the stimulation azimuthal plane was chosen according to the maximal neuronal response in the imaged plane. The inter-trial time interval for both bars and light spots was 7 sec. Stimulation order was randomized. All visual stimuli protocols were programmed using the Psychtoolbox (Brainard, 1997; Pelli, 1997) for Matlab and synchronized with the two-photon calcium imaging acquisition software (ScanImage, Pologruto et al., 2003) using an I/O TTL board (ActiveWire, inc).

Data processing

All the analysis were performed in MATLAB (Mathworks), including custom-made programs and built-in implementations of standard statistical and multivariate analysis algorithms, unless otherwise noted (the most important custom-made programs can be downloaded from http://www.zebrain.biologie.ens.fr/codes/index.html). All statistical tests applied were two-sample Kolmogorov-Smirnov tests, unless otherwise noted.

Analysis of imaging data

Registration

Calcium imaging videos were registered to remove slow in-plane (XY) drifts using the Image J plugin Template Matching (Tseng et al., 2012). We discarded videos with drifts in the ventral-dorsal direction (out-of-plane displacement, ~50 % of the videos). Movement artifacts were detected according to large deviations in the cross-correlation between successive frames. All frames with large deviations were then manually inspected. Due to the agarose elasticity, the imaging plane almost invariantly returned to its original position, after observing movement artifacts. If this was not the case, the complete experiment was discarded. Artifacts episodes rarely exceeded 2 consecutive frames in length. For the subsequent analysis, we did not include frames showing moving artifacts. In average, we detected 45 ± 36 movement artifacts per hour.

Segmentation

In a few cases we observed high-frequency non-Gaussian noise, most probably originated at the PMT (GaAsP, H1070 from Hamamatsu). This non-Gaussian noise was very rare, and was observed even when the laser was turned off as single frame, single pixels, significant intensity changes. To filter out these events, we calculated neuronal fluorescence traces by robustly averaging pixel fluorescence time series contained in single-neuron regions of interest (ROIs). To estimate this robust average, we first calculated, for all the imaging frames, the inter-frame fluorescence change coefficient of variation (CV) among the ROI pixels. For frames with CV > 1, we calculated the average fluorescence across pixels by leaving out the outlier pixel (i.e., pixels whose fluorescence change, z-scored across ROI pixels, were bigger than 1.5). ROIs were semi-automatically detected on a morphological basis by analysis of time-averaged pictures of the imaged region, *I*. We implemented a series of digital imaging processing techniques (Gonzalez and Woods, 2009) in a custom-made program that produced putative ROIs layouts that were afterwards manually curated. GCaMP3 is mainly localized in the cytosol, with minimal penetration to the cellular nuclei. Our algorithm first identified neuronal ROIs that corresponded to individual nuclei. The latter were detected by local fluorescence intensity wells. In order to flatten non-relevant intensity fluctuations in these minima, the eroded version of *I* was morphologically reconstructed under the mask given by *I*. Local minima were detected by applying a user-defined threshold to the extended-minima transform of the resulting image. Finally, to obtain the ROIs perimeters we took advantage of the high density of the SPV neurons. We calculated the euclidean distance transform of the local minima image, and we then performed a watershed segmentation to obtain the boundaries between neurons. The obtained ROIs were manually inspected and corrected when needed. ROIs typically included neuronal nuclei and a thin cytosolic surrounding ring, conservatively excluding the outermost cytosolic perimeter that could potentially be subjected of cross-neuron fluorescence contamination, due to the high neuronal density. This procedure gave similar results to fully-manual ROI selection, accelerated the process by ~5-fold and minimized the effect of user subjectivity.

Inference of fluorescence events associated to neuronal activity

The method described here infers the statistical significance of single-neuron calcium dynamics in an adaptive and unsupervised manner. Conceptually, it considers that any event in the fluorescence time series data belongs to either neuronal activity process, *A,* or to an underlying noisy baseline, *B*. In order to discriminate, with a desired degree of confidence, between these two sources, we built a data-driven model of *B*, and imposed biophysical constraints of the fluorescent calcium indicator. We then applied a Bayesian odds ratio estimation framework, as explained below, to obtain the significant *ΔF/F* transients. Non-significant portions of the *ΔF/F* traces was set equal to 0 for all subsequent analysis.

Raw fluorescence datasets consisted of the fluorescence time series of N neurons sampled at T discrete time points, represented as N x T matrices. In the present work, N = ~1000 and T = ~20000. We calculated a smooth estimate of the fluorescence baseline for each neuron, b_{slow}, by computing the 30-seconds-long running average of the 8th percentile of the raw data (Dombeck et al., 2007). This estimate reflected slow fluctuations unrelated to the fast calcium transients. We then subtracted from the raw fluorescence data the corresponding b_{slow} and the result was further divided by the latter in order to obtain a rectified estimate of the relative fluorescence change, *ΔF/F*. To infer the noise magnitude of process *B,* we calculated the variance of *ΔF/F* baseline. A neuron's *ΔF/F* typically presented a positively skewed distribution (**Figure S1A**). The latter peaked at a value μ, with a long positive right heavy-tail populated by neuronal calcium events. The most frequent value of the time series, μ, represented a constant residual value of *ΔF/F* ($\mu = 0.23 \pm 0.06$ for a representative dataset) product of an underestimation of b_{slow}. The *ΔF/F* time series of each neuron were therefore recalculated after correcting b_{slow} by the factor ($1+ \mu$). Samples represented by the left tail were negative *ΔF/F* deflections from the baseline produced by *B*, hence not related to neuronal calcium events. A robust estimate of the standard deviation (s.d.) of *B*, σ_{noise}, can be obtained if we consider that *B* is a Gaussian stochastic process, allowing us to fit the left *ΔF/F* tail with a normal distribution of mean μ and s.d. σ_{noise}. This assumption seemed valid due to the accuracy of the calculated fits ($r^2 = 0.995 \pm 0.002$ for a representative dataset) (**Figure S1A**).

Single-neuron *ΔF/F* time series had diverse amplitude scales and noise levels, as quantified by the distribution of their s.d., σ, and of σ_{noise} (**Figure S1B**). Therefore, in order to unbiasedly compare the dynamics across neurons, we needed to adaptively normalize the multivariate dataset to standardize the variance across the multiple time series. A satisfactory normalization was obtained by dividing each time series by the corresponding σ_{noise}, defining a dimensionless quantity $Z_{n,i}$ that approximates the signal-to-noise ratio of the neuron n at the time sample i. The $Z_{n,i} \rightarrow Z_{n,i+1}$ transitions between negative values should again be the product of *B*. Consequently, we used the lower left quadrant data (left in **Figure S1C**) to estimate the covariance matrix *K* of the baseline noise *B* and model it as a bivariate Gaussian process with 0 mean and covariance *K*. The off-diagonal terms of *K* were negligible (0.03 ± 0.01), suggesting the near-independence of successive samples of the noise process. In the left plot of **Figure S1C**, the noise model *B* was compared to the actual data. As expected, a great portion of the $Z_{n,i} \rightarrow Z_{n,i+1}$ transitions between large positive values (upper right quadrant) were not accounted by *B*, since they corresponded to large positive excursions of the time series that represent the calcium transients of interest.

Since any event could only be attributed to *A* or *B*, consequently, given a particular $Z_{n,i} \rightarrow Z_{n,i+1}$ transition, the *baseline noise posterior probability* and the *activity posterior probability* sum up to one (equation 1)

$$p(B|Z_{n,i}Z_{n,i+1})+p(A|Z_{n,i}Z_{n,i+1})=1 \qquad (1)$$

To assess the source of any $Z_{n,i} \rightarrow Z_{n,i+1}$ transition, we calculated the odds that could belong to *B,* relative to the odds produced by *A*, namely the *posterior odds* for *B* against *A*, which is the ratio between the two terms in equation 1. By forcing a lower bound to these odds, we could estimate the confidence bound of considering a given $Z_{n,i} \rightarrow Z_{n,i+1}$ transition as a neuronal activity event (equation 2)

$$\frac{p(B|Z_{n,i}Z_{n,i+1})}{p(A|Z_{n,i}Z_{n,i+1})} \leq \gamma \qquad (2)$$

Which, using equation 1 reduces to

$$p(B|Z_{n,i}Z_{n,i+1}) \leq \frac{1}{1+\gamma^{-1}} \equiv \beta \qquad (3)$$

In the present work, we chose a β value of 0.05, implying posterior odds of 19:1 against noise ($\gamma^1 = 19$) and a confidence of 95 % on the classification of the $Z_{n,i} \rightarrow Z_{n,i+1}$ transition as a neuronal activity event. Therefore, we only needed to estimate the leftmost term in equation 3, the baseline noise posterior probability. Using Bayes' theorem (equation 4), the latter can be decomposed as in equation 5.

$$P(X|Y) = \frac{P(X)}{P(Y)} \cdot P(Y|X) \qquad (4)$$

$$p(B|Z_{n,i}Z_{n,i+1}) = p(B) \cdot \frac{p(Z_{n,i}Z_{n,i+1}|B)}{p(Z_{n,i}Z_{n,i+1})} \qquad (5)$$

The first term on the right hand side, the *prior probability of noise*, should be close to one since the calcium transients are relatively rare (*p(B) >> p(A)*). However, its actual numerical value would not change qualitatively the inference procedure, since it is just an overall scaling factor. The denominator of the second term, the *probability density of data transitions*, can be estimated directly from the measured dataset. Finally, the numerator of the second term, the *probability density of data transitions, given the baseline noise process*, will be approximated by the already described noise model shown in the left plot of **Figure S1C**. The density distributions of the two latter terms were smoothly estimated by means of a bivariate locally adaptive density estimation procedure, using the dataset and a run of the noise model, respectively. With all these variables we could then infer the *posterior odds* for *B* against *A* for any given $Z_{n,i} \rightarrow Z_{n,i+1}$ transition in the data (equation 2).

In an effort to rule out non-neural-activity related $Z_{n,i} \rightarrow Z_{n,i+1}$ transitions that can not be explained by the noise process *B* (non-Gaussian noise in the detection process, most probably originated at the PMTs), we imposed a final biophysical constraint to the inference procedure. This constraint is given by the decay time constant of GCaMP3 (Yamada et al., 2011), $\tau_{\text{decay}} = 275$ ms (mean half-decay time of ~190 ms). The exponential decay of the calcium transients indicated that the relationship between the fluorescence signals of two consecutive imaging frames separated by the inter-frame time interval $\Delta t_{\text{imaging}}$ should be bounded by equation 6.

$$e^{\left(\frac{-\Delta t_{imaging}}{\tau_{decay}}\right)}(Z_{n,i}-1) \leq Z_{n,i+1}+1 \qquad (6)$$

As observed in equation 6, in practice, when setting the threshold, we allowed for a noise corruption of value 1 (one σ_{noise}) of each $Z_{n,i}$. These limits imposed a straight bound in the amplitudes of $Z_{n,i} \rightarrow Z_{n,i+1}$ transitions. The combination of this time constant bound together with the estimated map of posterior odds results in a range of transitions that both respect the temporal dynamics of GcaMP3 and are inferred to be produced by neuronal activities with at least 95 % confidence (right plot in **Figures S1C** and **S1D**).

Examples of *ΔF/F* transients considered as significant by this method are shown in **Figures 1C**, **2A** and **S1D**.

It is instructive to compare this method of posterior odds thresholding to the popularly used *likelihood ratio test*, which optimally minimizes an expected loss function of the classification (Dayan and Abbott, 2001). In contrast, the method presented here, essentially puts a limit to the quantity of false positives that we were able to accept (at the expense of possible false negatives). Using Bayes' theorem again (equation 4), we expanded *posterior odds* for *B* against *A* (equation 7).

$$\frac{p(B|Z_{n,i}Z_{n,i+1})}{p(A|Z_{n,i}Z_{n,i+1})}=\frac{p(B)}{p(A)}\cdot\frac{p(Z_{n,i}Z_{n,i+1}|B)}{p(Z_{n,i}Z_{n,i+1}|A)} \qquad (7)$$

The first term in the right hand of equation 7 is the *prior odds*, which reflects our *a priori* expectation for the odds without taking into account any particular measurement, and the second is the *likelihood ratio* which modulates the naive prior inference by the ratio of probabilities for a transition given either the *A* or *B* process. As mentioned, the latter term could be used to infer if any given transition is related to neuronal activity by estimating the corresponding likelihood ratio (below or above a certain threshold parameter η). However, for that purpose, we should build a model for the *A* process, an impossible task due to the dependence on the input. Anyway, equation 7 indicates that the likelihood ratio and the posterior odds were equal, up to the constant factor prior odds, that does not depend on the measured data. This means that any inference based on the posterior odds (the current method) is qualitatively similar to the one that could be performed through the likelihood ratio test, albeit an overall scaling factor of the confidence value.

Determination of neurons responsive to visual stimulation

Neuronal activity patterns evoked by visual stimulation were quite variable across trials. Therefore, for each particular stimulation, we averaged across trials the neuronal responses within a 2 s time window after the trial onsets, and z-scored this average vector across neurons. We considered a neuron as consistently responsive to a stimulation if it had an average response z-score bigger than -1 and reacted in at least 50 % of the trials. We define a visually induced *neuronal group* as the neuronal population that responded in this manner to a given stimulation.

Calculation of neuronal azimuthal tuning curves

The neuronal spatial (azimuthal) tuning curves (**Figure 1D**) were estimated by the normalized sum of 10^{o}-wide Gaussian curves centered at the 4^{o}-light-spot azimuthal visual field locations that induced neuronal responses. The obtained curves were normalized to 1. Smaller Gaussian widths (4^{o}-9^{o}) produced comparable but less smooth results.

Calculation of neuronal direction selectivity

Neuronal direction selectivity (**Figure 2B**) can be quantified as a planar vector whose norm indicates tuning strength and its angle directional preference. For each neuron responsive to bar stimulation, we calculated their up-down and left-right selectivities as the difference of their average neuronal responses to bars moving in opposite cardinal directions (up-down and left-right, respectively), divided by their sum. Finally, we estimated the direction selectivity vector of each neuron as the vectorial sum of their up-down and left-right selectivities.

Normalization of neuronal anatomic coordinates

In order to compare topographical features across different tectal planes or larvae, we developed a method to express neuronal positions in anatomically normalized tectal coordinates. Tectal anatomy possesses two evident structuring axes (**Figure 1B**), the rostro-caudal and a medio-lateral, which also play a role in tectal functional organization (Burrill and Easter, 1994; Niell and Smith, 2005; Stuermer, 1988). We therefore chose to project and normalize the Cartesian neuronal centroid coordinates over these axes. Due to their curvature, this can only be accomplished in an approximate manner, since the problem becomes ill-posed at regions of marked axis curvature where a point can be equally mapped to two distinct axis positions. To overcome this problem, we estimated a neuron's normalized coordinate at problematic axis segments by choosing the projection over the axis position closest to the neuronal centroid. Despite the fact that the framing of the imaged videos could not be guaranteed to be always exactly the same, this normalization procedure could satisfactorily reveal functional topographic principles in the larva's optic tectum, as demonstrated by the clear representation of the retinotopic tectal map (**Figure 1G**). Axes were automatically calculated after the manual delineation of specific tectal landmarks: the separating tectal midline, and both SPV-neuropile and tectum-cerebellum boundaries. When participating in *N* assemblies, the neuron was represented *N* times with a slight random displacement in its medio-lateral position.

Detection of neuronal assemblies

Examination of calcium event histograms of neuronal population spontaneous activities (**Figure 3B**) revealed periods of synchronous calcium events. To assess the significance of these events, we determined a threshold corresponding to the maximal neuronal population synchronization obtained, with 99 % confidence, on 1000 simulations of surrogate datasets with shuffled neuronal inter-activation intervals (*IAI*). Events of collective neuronal activation surpassing this threshold were considered as significant. Significant events were frequently observed in all experiments, therefore we designed a procedure to determine the neuronal identity during the synchronous calcium event episodes.

In the present work, we defined a neuronal assembly as a group of neurons with significantly correlated activation dynamics, either spontaneously (spontaneous assemblies) or induced by stimulation (visually induced assemblies). This does not imply anatomical connection between the concerned neurons, but represents clusters of neurons that are consistently co-activated and therefore could function as a neuronal processing module. Importantly, it was essential to identify flexible and dynamic neuronal assemblies, engaged and disengaged in a moment-to-moment basis, according to neuronal circuit states. Therefore, any procedure designed to detect them should satisfy important conditions. The method should not only search for neurons whose activations are correlated in average along the entire experiment, but must also be capable of defining clusters of neurons episodically activated in synchrony. Furthermore, since a given neuron could be related to diverse functional groups, the algorithm should be able to define non-exclusive assemblies (i.e., allow for potential overlap between the detected clusters).

With these conditions in hand, we applied a procedure that relies on previously proposed techniques (Lopes-dos-Santos et al., 2011; Peyrache et al., 2010). Our procedure first represented the complete time series of neuronal population activities in a space of reduced dimensionality through principal component analysis (PCA). We then used a second algorithm for the partitioning of this space by means of non-orthogonal factor rotation, *promax* (Hendrickson and White, 1964).

In order to normalize variance across neurons and avoid biasing the principal components (PCs) towards the most active neurons (i.e., the ones with the largest variance), we worked on z-scored neuronal time series. Under these conditions, PCA will mainly represent neuronal activity covariance. Dataset dimensionality reduction was obtained by only keeping PCs with eigenvalues bigger than $\lambda_{\max}$, a theoretical lower bound to the eigenvalues of informative PCs, given by the Tracy-Widom corrected Marčenko-Pastur distribution (Peyrache et al., 2010; Tracy and Widom, 1992) (equation 8)

$$\lambda_{max} = \left(1 + \sqrt{N/T}\right)^2 + N^{-2/3} \qquad (8)$$

In practice this procedure reduced data dimensionality by ~280 fold (from ~14000, the number of imaging frames, to ~50 dimensions, the number of significant PCs).

Each significant PC could be used to isolate clusters of correlated neurons (Peyrache et al., 2010) (top panels in **Figure S2A**), however, since assemblies do not need to be exclusive (they may share neurons), we could relax the PCA orthogonality condition (Lopes-dos-Santos et al., 2011). Therefore, to delineate the assemblies, we decided to work on a space of obliquely rotated components (*promax*), that tended to sparsely concentrate the PC loadings along non-orthogonal rotated PCs (middle panels in **Figure S2A**). An example of the effect of this procedure is presented in **Figures S2A** and **S2B**. Already in PC space, we observed some structure, with groups of neurons presenting rather similar PC loading curves. This structure is greatly enhanced after component rotation (**Figure S2B**). The distribution profiles of loadings along the rotated PCs, enabled us to use them as linear discriminators delineating clusters. Hence, after z-scoring loadings on rotated PCs, a neuron was included in a particular assembly defined by a rotated PC if its z-scored loading on that rotated PC exceeded a threshold value. This threshold was easily estimated across experiments as the first robust minima in the distribution of z-scored maximal neuron loadings (usually corresponding to a value of ~2, **Figure S2C**). Since the relaxation of orthogonality condition could change the relevant dimensionality of the data (the number of latent dimensions), some rotated PCs could potentially extensively overlap. This would result in redundant clusters. Therefore, we merged clusters determined by two rotated unitary PCs if the dot product of the latter exceeded 0.6. As a final constraint, only significantly correlated and synchronous clusters were kept ($p < 0.05$, compared to null models (see *Null models for analysis of assembly significance*). In practice, assembly merging and the correlation constraint reduced in less than ~10 % the number of assemblies found by the original rotated PCs.

In practice each significant collective neuronal activation observed in the histogram of population activity corresponded to the activation of one or more neuronal assemblies.

For ongoing spontaneous assemblies we used the entire one hour of the total imaged neuronal population. For visually induced assemblies we only considered population activities during the stimulation period (a 5 s time window starting at the onset of the stimulus)

Comparison between the performances of the *PCA-promax* and *hierarchical clustering* algorithms

Attempts to cluster spontaneous network activity directly from neuronal activation time series by means of widely used algorithms like *k-means* or *hierarchical clustering* either resulted in clusters that could not be validated or failed to reveal any significant structure. This is most probably explained by the high dimensionality of the data space, where data become extremely sparse and the concept of distance between points may not even be qualitatively meaningful (Aggarwal et al., 2001), which seriously undermines the performance of clustering algorithms (one of the "curses of dimensionality"). We thus opted to reduce dimensionality of the spontaneous activity data prior to the clustering implementation. Since the *PCA-promax* procedure has also an initial dimensionality reduction step through PCA, we performed this same PCA step on the data before *hierarchical clustering*. In this way, we matched the difficulty of the clustering problem for both *hierarchical clustering* and *PCA-promax* techniques, allowing for the comparison of their performances. Thus, the dimensionality of the spontaneous activity data was reduced by working on PC space and keeping only the significant PCs (equation 8). We then calculated the matrix of pair-wise euclidean distances between neurons in this dimensionality-reduced PC space, *D*, for all experiments.

We performed standard complete-link agglomerative *hierarchical clustering* of this distance matrix *D,* obtaining a hierarchical clustering tree for each experiment. The problem was now reduced to choosing a horizontal cut through these trees that produced valid clusters. To do this, we adopted a standard clustering validation method (Theodoridis and Koutroumbas, 2009), similar to Bathellier and colleagues (Bathellier et al., 2012). Varying the number *k* of clusters obtained by cutting the clustering tree, we quantified the validity of the clusterings results by means of the normalized Hubert's Γ statistic (equation 9; **Figure S2D**)

$$\Gamma_k = \frac{2}{N(N-1)\sigma_D \sigma_C} \sum_{p=1}^{N-1} \sum_{q=p+1}^{N} (D_{p,q} - \mu_D)(C^k_{p,q} - \mu_C) \quad (9)$$

where N is the number of neurons, C^k is a matrix associated with clustering in k clusters, defined as $C^k_{p,q}=1$ if neurons p and q are in the same cluster and $C^k_{p,q}=0$ otherwise, while μ_X and σ_X are the means and standard deviation of matrix X, respectively. The matrix C corresponds then to the matrix D that would be obtained in the ideal case of having identical spontaneous activities across neurons of the same cluster and uncorrelated activities for neurons belonging to different clusters. Therefore, Γ_k is analogous to a correlation coefficient between D and the matrix C^k that represents perfect clustering in k clusters, and its values range between -1 and 1, where 1 indicates that D completely matches C^k.

The Γ_k curve for spontaneous activity datasets typically showed a clear and unique maximal peak, for the range of k tested (from 1 to 80). The final number of clusters chosen for the clustering procedure, k^*, corresponds to the value that maximizes Γ (**Figure S2D**). To test the statistical significance of the Γ_{k^*} obtained for the spontaneous data, we controlled against a reference consisting of a collection of 1000 randomized surrogate datasets and calculated their performance in this clustering procedure, Γ^{null}_{k*}. To build this surrogate set while keeping the overall statistical structure in the data, we replaced the spontaneous data in the PC space of reduced dimensionality by a set of data randomly drawn from a uniform distribution over the hypercube aligned to PCs that encloses the real data (Tibshirani et al., 2001). We then tested against the null hypothesis that the surrogate dataset was capable of producing a Γ^{null}_{k*} equal or bigger than Γ_{k*}. All the final clusterings were highly significant ($p < 10^{-5}$; **Figure S2D**).

Despite the great importance of k^* for the clustering procedure, there was no simple trend in the relationship between k^* and Γ_{k*} (**Figures S2E** and **S2F**), which indicates that the performance of the clustering procedure was not a simple consequence of choosing higher or lower values of k^*.

We observed that the performance of the clustering was significantly better for the *PCA-promax* procedure compared to *hierarchical clustering*, as measured by both Γ (**Figure S2G**; 0.22 ± 0.12 for *hierarchical clustering* and 0.41 ± 0.06 for *PCA-promax*, $p < 10^{-5}$) and the *Davies-Bouldin index* (see below for definition; **Figure S2H**; 7.78 ± 1.75 for *hierarchical clustering* and 6.66 ± 1 for *PCA-promax*, $p = 0.018$). Both methods gave significantly valid clusterings, as compared to the surrogate datasets. Moreover, significant positive correlations were ~5-fold more represented in the *PCA-promax* clusters than in the *hierarchical clustering* clusters (**Figure S2I**), which indicates that *PCA-promax* clusters are more correlated.

Determining the match between activation patterns through the *matching index*

We implemented the *matching index* (*MI*) to quantify the degree of similarity, at the neuronal level, between any given pair of network activation patterns, either visually induced or spontaneous. This index was used to quantify the degree of topographic match between target neuronal patterns representing visually induced neuronal groups and spontaneous assemblies (**Figure 7D** and inset in **Figure 7E**). Furthermore, the *MI* was also used for the analysis of the temporal dynamics of network activation, quantifying the match of neuronal activations between the time-series of spontaneous network activation patterns and given target patterns consisting of either visually induced neuronal groups (**Figures 3C** and **3D**) or spontaneous assemblies (**Figure 4A**).

The *MI* (also known as *Dice coefficient*) was previously used to evaluate the degree of similarity in the connection patterns of brain regions (Hilgetag et al., 2002; Sporns et al., 2007). It is defined as

$$MI_{ij} = 2\frac{|Pat_i \cap Pat_j|}{|Pat_i| + |Pat_j|} \qquad (9)$$

where both Pat_i and Pat_j are binary neuronal activation patterns (a binary vector representing the imaged neuronal population, with ones indicating active neurons and zeros for the silent ones). Norms are equal to the number of ones in each vector. The *MI* quantifies the proportion of neuronal activations that are common to both patterns with respect to the total number of activations present in both patterns. It is valued between 0 (no overlap in activations) and 1 (perfect overlap in activations). The *MI* aims to estimate the number of “hits” between neuronal activations (common ones in the vectors) without specifically considering as a “hit” a match between silent neurons (common zeros), opposed to the popularly used *Hamming distance*, which can become problematic when considering the match of sparse binary vectors. For the evaluation of the topographic match between the target patterns of visually induced neuronal groups and spontaneous assemblies (**Figure 7D** and inset in **Figure 7E**), Pat_i is the binary target pattern of neuronal group *i,* and Pat_j is the binary target pattern of spontaneous assembly *j*. When quantifying the temporal dynamics of neuronal activation overlap between momentary spontaneous network activation patterns and visually induced neuronal groups (**Figures 3C** and **3D**), Pat_i is the binary spontaneous network activity pattern of imaging frame *i,* and Pat_j is the binary target pattern of neuronal group *j*. Finally, when considering the activation temporal dynamics of spontaneous assemblies during spontaneous network activity (**Figure 4A**), Pat_i is again the binary spontaneous network activity pattern of imaging frame *i,* and Pat_j is the binary target pattern of spontaneous assembly *j*.

To estimate the significance of *MI*s, we used the hypergeometric distribution ($p < 0.01$). Under the null hypothesis of independent neuronal activations, this is a discrete distribution that describes the probability of having k "hits" (common neuronal activations) with n target neuronal activations in a population of N neurons showing K activations at a given moment. Therefore, it allowed us to estimate the probability of observing a given activation match by chance, with neurons independently activated.

The overall *activation level* (*AL*) of an assembly is the time integral of its *MI*.

We found that the *MI* was more reliable than the method proposed by Peyrache and colleagues (Peyrache et al., 2010) to quantify the activation dynamics of neuronal assemblies. They suggested to project population activity over the vectors defined by the PCs, which in our case would correspond to the *promax*-rotated PCs. However, we found this process to be unsatisfactory for our data, since instances of activity bouts engaging large fractions of the neuronal population resulted in considerable projections over several PCs, artificially segmenting these generalized population activations into several smaller neuronal subsets, hence undermining the specificity of this activation measure.

Generation of null models and *topographical null models* for analysis of the significance of assembly's features

Random shuffled null models

To assess the significance of the topographic and dynamic features of the neuronal assemblies, we compared them against surrogate assembly null models. For this purpose, we permuted the indexing of the entire neuronal population for each experiment. These permutations enabled us to create a set of shuffled surrogate assemblies for each experiment by using the original dataset clustering (i.e. the original non-permuted neuronal assemblies) but sampling neurons according to the permuted indexes. For each experiment, we generated a dataset of null models containing 1000 permutation rounds. This procedure randomized only the assemblies topographies, while keeping intact every other feature of a given dataset (e.g. the particular overlaps between assemblies, the number of neurons per assembly, the topographical position and the activation time series of each neuron). The preservation of these properties enabled testing the specificity of the neuronal associations present in the assemblies.

The significance of a given assembly feature observed in the data was quantified with respect to the null model sets by calculating the probability of obtaining in the null models a feature value at least as extreme as the one measured in the data (*p*-value).

Topographical null models

To test the specificity of spontaneous assemblies for functionally related neurons while controlling for their topographical compactness, we imposed to the null models the additional constraint of conserving the distribution of relative pair-wise physical distances between neurons found in the original assemblies (*p(d);* see **Figure 4J**). Each spontaneous assembly was assigned to one of the tecti according to their topographical centroids, and we built for each assembly a set of 100 *topographical null models* (TNMs) in the contralateral tectums to avoid any chance of completely or partially reproducing the original assemblies. To build the TNMs, for a given spontaneous assembly with n neurons, we randomly chose a neuron in the contralateral tectum and iteratively added n-1 neurons to the assembly's TNM in a way that conserved the assembly's *p(d)* as best as possible. To this end, at a given step j of the iteration (when the TNM has already j-1 neurons), we added a new neuron whose pair-wise distances to the j-1 TNM neurons were most similar (in a mean-squared-error sense) to any given set of j-1 distances present in the original assembly. Furthermore, we also respected, for each TNM assembly, the proportion of neurons in either tectum as observed in the original assembly. When the iteration of a TNM was over, we only kept the TNM if its *p(d)* was statistically non-different from the original assembly's *p(d)* (p-value>0.05). The average p-value for all TNMs was 0.86 ± 0.22; n=53400 TNMs.

We also used this procedure to build TNMs for light-spot-induced neuronal groups to test the specificity of the transient spontaneous emergence of spatially localized visual representations (**Figure S3D**).

Compactness index* and *relative area

Topographic compactness and dispersion of assemblies was quantified according to the *relative area* and the *compactness index*. These are dimensionless, data-independent, normalized statistics that enabled us to unbiasedly compare across experiments.

We first estimated the smooth assembly topography density maps using morphological masks corresponding to assembly patterns, and smoothed the masks with a running bi-dimensional Gaussian of width proportional to the number of assembly neurons (**Figure S5C**). The region occupied by the assembly was defined as the region encompassed by the contour line (i.e., the isoline, green line in **Figures S5A** and **S5C**) that corresponds to a density value of half the maximal density.

The *Relative area* of an assembly was defined as the area of the region occupied by the assembly divided by the area of the tectum on which the assembly resides. This index estimates the tectal area occupied by the focus of activation of an assembly.

The *compactness index* is designed to quantify the neural density and the packing of the assembly. To calculate it, we drew a circle of an area equal to the area of the region occupied by the assembly, centered at the peak assembly density map. We defined the *compactness index* as the proportion of assembly neurons that reside inside this circle (**Figure S5A**).

Multidimensional Scaling

To validate and further support our data on the optic tectum network dynamics, we applied multidimensional scaling (MDS, Kruskal and Wish, 1978). This non-linear technique maps each neuronal time series, represented as a point in the network's high-dimensional space, to the bi-dimensional projection that best preserves the between-point distances. These distances are directly proportional to the pair-wise similarity of neuronal dynamics. Therefore, it is a useful visualization tool of the organization structure in population dynamics. We applied the non-classical MDS algorithm on dissimilarity matrices of the z-scored neuronal activity time series, calculated with the euclidean distance metric, with Kruskal's normalized stress-1 goodness-of-fit criterion.

We qualitatively confirmed the validity of the detected assemblies by coloring dots (neurons) in the MDS mapping of neuronal population activity according to the assemblies partitioning. We could clearly see the formation of clusters of similarly-colored dots (**Figures S4A**-**S4C**). Interestingly, using the color code of the spontaneous assemblies to depict the neurons in the stimulated conditions, we were still able to observed a reasonable description of the network dynamics during light-spot stimulation and, to a lesser degree, during moving bar stimulation (**Figures S4D** and **S4E**).

Davies-Bouldin index and *clustering quality index*

The Davies-Bouldin index (Davies and Bouldin, 1979) enabled us to quantitatively validate individual assemblies, since it measures the degree of separation of a particular cluster from the rest of the data. If M_{ij} is the separation between the centroids of clusters i and j, and S_i is the scatter of cluster i, the Davies-Bouldin index of cluster i, DB_i, is defined as the worst-case scenario of the ratio between these variables (equation 10)

$$DB_i = \max_{j:i \neq j} \frac{S_i + S_j}{M_{ij}} \qquad (10)$$

The cumulative distributions of the Davies-Bouldin indexes for the assembly partitionings under different conditions is presented in **Figure S4F**.

Since this index is inversely proportional to the degree of cluster validity, a particular partitioning is of better quality, if its cumulative distribution peaks sooner and steeper. Therefore, to quantify the validity of a particular assembly partitioning, we measured the Davies-Bouldin indexes at which the cumulative distribution peaked with respect to the null model. This difference would then represent the level of collective dynamics structure gained in comparison to a random partitioning. We then defined the *clustering quality index* as the area between the cumulative distributions of the Davies-Bouldin indexes for the dataset of interest and its respective null model. As measured by this index, clusters formed by spontaneous assemblies perform only 7 % worse than the light-spot-stimulated clusters in explaining the clustering structure of the light-spot-stimulated neuronal-population data, while for the moving-bar stimulation responses the decrease in performance was of 36 % (**Figure S4G**). We observed that a 7 % decrease in *clustering quality index* performance could be reproduced by introducing 10 % of errors in the spontaneous partitioning (randomly replacing 10 % of the neurons within each spontaneous assembly, **Figure S4G**).

Signal and noise correlations

The *signal correlation* is a measure of the tuning similarity of two neurons, and was calculated as the Pearson's correlation between the mean responses of each neuron to each light-spot stimulus position in the larva's visual field. The mean neuronal response to a stimulus position was the across-trial average of neuronal responses in a 2-s time window after stimulation trial onset.

The *noise correlation* (also known as the *spike count correlation*) is the Pearson's correlation coefficient of the evoked responses of two neurons to repeated presentations of a particular stimulus: it captures shared trial-to-trial variability. For each light-spot stimulus position in the larva's visual field, trial responses were computed in a 2-s time window after stimulation trial onset and these trial responses were normalized to a mean of zero and unit variance (z-score). We then calculated *noise correlation* after combining responses to all light-spot stimuli.

Eye enucleations and retina laser ablations

For this purpose we embedded 8 dpf larvae in 2 % low-melting agarose and immersed them in high-calcium Ringer's solution (in mM): 116 NaCl, 2.9 Kcl, 10 CaCl2, 5 HEPES; pH 7.2; at ~13° C for anesthetic purposes.

The single-eye enucleations were performed using a curved insect pin. Following the procedure, we freed larvae from agarose and, after one hour, they were returned to normal embryo medium and left to recover.

For the laser ablations, we embedded larvae laying on one of their sides and, focusing on 50 µm x 50 µm areas of the crystalline lens, we scanned the retina for 5 seconds with a Ti:Saphir pulsing laser tuned to 920 nm at 12 mW. Larvae were then freed and left to recover in embryo medium.

Both procedures (3 eye enucleations and 2 ablations) were performed between 24 h and 48 h before the imaging experiments. Only healthy and well recovered larvae were used for the experiments. Among these, we only took into account larvae that did not show contralateral visual responses induced by stimuli presented to the affected eye, but did exhibit contralateral normal responses induced by visual stimulation of the intact eye.

Spontaneous assemblies as preferred states

We were interested in studying how the activation probability of a neuron participating in a given assembly, is modulated by the spontaneous emergence of population activation profiles of the imaged tectum that gradually resembles the pattern associated with the concerned assembly.

To test that the activation probability of a neuron is modulated by the spontaneous emergence of its neuronal assembly, we took advantage of the approach used by Tsodyks and collaborators (Tsodyks et al., 1999), but for single-neurons instead of voltage-sensitive dye imaging voxels. For the pattern of a given assembly j, Pat_j, the matching between Pat_j and the entire imaged network activity at frame i, Pop_i (binary population activity profile) was quantified by their linear correlation. Then, for all the neurons of an assembly, we calculated the histogram of correlation coefficients observed during the complete recording session and the same histogram but only at frames at which the tested neuron was active. To estimate the effect of the population-assembly pattern match on the activation probability of any neuron of an assembly, we divided the second histogram by the first one (Bayes' theorem). Importantly, to avoid any bias, the tested neuron was never included in the population activation profiles nor in the target assembly patterns. This permitted us to isolate the effect of the collective activation of its assembly partners. In practice, since some histograms were quite sparse, to increase the robustness of calculations, we chose non-homogeneous bin widths so as to include 2 % of the correlation coefficients in each successive bin. Using this method, we could observe two distinctive "facilitation" patterns: linear and step-like non-linear (**Figures 6A**, **6B** and **S7A**).

Imbalance index, analysis of interactions between light-spot-induced responses

To quantify the interaction level between two neuronal groups induced by the two nearby light spots we used *linear decomposition* and *linear discriminant analysis*.

First, we mapped the neuronal responses to individual 4° light spots (10 trials each), and to two simultaneous 4° light spots separated by azimuthal distances of Δ10°, Δ20° and Δ30° (20 trials each; **Figure 6D**). We then estimated how well trial responses to the simultaneous presentation of two light-spots could be explained by a balanced linear summation of two template patterns consisting of the across-trial average responses to each individual light spot presented separately.

For this purpose, we used a standard least square linear fitting algorithm (Moore-Penrose pseudoinverse method) to linearly decompose single-trial responses (of both single and simultaneous light-spot stimulations) with respect to the two average single-spot activation templates (e.g., the red and green bar plots shown in **Figure 6D**) This algorithm calculated the linear weights for the average single-spot activation templates that best described each stimulation trial.

This allowed us to express the importance of each of the templates in explaining each trial response by an *imbalance index*, which is defined as

$$Imbalance\,index = \frac{w_1 - w_2}{w_1 + w_2} \qquad (11)$$

where w_1 and w_2 are the trial response decomposition weights associated with each template (where 1 and 2 respectively correspond to the most rostral and the most caudal light spot). This index ranges between -1 and 1, where 0 indicates exact balanced linear summation of both templates, while 1 and -1 respectively indicate that only the most rostral or the most caudal template were enough to explain the trial response (winner-takes-all competitions).

As observed in red and green *imbalance index* distributions in **Figure 6F**, this procedure was successful in classifying single-light-spot trial responses with respect to the average single-spot activation templates (see also red and green data points in **Figures 6E** and **6F**). Therefore, this procedure was capable of discriminating between both templates, and we used it to quantify the contributions of these templates to explain the simultaneous-light-spot trial responses (yellow data points and corresponding *imbalance index* distributions in **Figures 6E** and **6F**).

However, since we observed across-trial variability in the visually induced neuronal responses for single-light-spot stimulation, the index could take non-zero values during simultaneous stimulation with the 2 light spots even if there is no interaction between the neurons responding to either individual light-spot. Therefore, as a control, we estimated the expected indexes that we would obtain given a balanced linear response summation scenario, by analyzing all the possible pair-wise sums of single light-spot trial responses (black lines in **Figures 6F** and S7**E**). This gave us a way to estimate the expected distribution of *imbalance indexes* in the linear summation condition with no interaction between the neuronal groups, given the observed across-trial response variability for single-light-spot stimulation, and to test the statistical significance of the indexes obtained during simultaneous-light-spot stimulation.

Normalized azimuthal tuning of spontaneous assemblies

The azimuthal tuning of a spontaneous assembly is defined as the sum of the azimuthal receptive fields of its composing neurons.

Since all the tested azimuthal locations may not be homogeneously represented by the imaged neuronal population, some azimuthal tuning may be observed even in assembly null models. We controlled for this bias by calculating, for each experiment, the mean azimuthal tuning across the null models. To obtain the assemblies' normalized tuning (*NT;* **Figure 7A**) curves, we subtracted the latter from the assemblies' receptive fields.

To define the visual field regions where spontaneous assemblies globally showed significant *NTs* and *AL*s, we compared to the *NT*s and *AL*s of average null models. We observed that lateral right (*LR*, -50° to -33°), lateral left (*LL*, 25° to 50°) and rostral (-22° to 18°) visual field regions showed significantly different behaviors when compared to the corresponding null models (see **Figure 7B**). The mean *NT*s were of $(2.2\pm0.8)\text{x}10^{-4}$ for *LR*, $(3.4\pm0.9)\text{x}10^{-4}$ for *LL*, and $(-2.2\pm1.4)\text{x}10^{-4}$ for rostral. *LR* vs. rostral: $p<10^{-5}$, *LL* vs. rostral: $p<10^{-5}$, *LL* and *LR* not significantly different for all equivalent angles, $p>0.05$. The mean *AL*s were of 3.3±0.2 for *LR*, 3.7±0.3 for *LL*, and 2.9±0.2 for rostral. *LR* vs. rostral: $p<10^{-5}$, *LL* vs. rostral: $p<10^{-5}$, *LL* and *LR,* for all equivalent angles: $p=0.017$.

Direction-selectivity tuning of spontaneous assemblies

An assembly direction selectivity vector was defined as the vectorial sum of the direction selectivity vectors of its composing neurons. To test for statistical significance, we calculated the smooth bi-dimensional distributions of null model direction-selectivity vectors and estimated the stimulated assemblies *p*-values (**Figure S3G**).

Prey-detection behavioral assays

8 dpf old larvae were transferred to 16 mm round wells and left to habituate for at least 1 hour. Following the habituation, low densities of *paramecia* (*Paramecium multimicronucleatum*) were added. Videos were acquired at 200 Hz using a high-speed camera (Redlake MotionScope M3, 1280 x 1024 pixel resolution) connected to a binocular (PZMTIV-BS, World Precision Instruments). The wells were illuminated with wide-field white light and infra-red LEDs. The latter, for video purposes.

We defined a *paramecia* detection event (n = 60) as the moment at which larvae either generated converging-eye movements or the first J-turn movement (Bianco et al., 2011; McElligott and

O’malley, 2005) towards the target (*paramecia*) following a prolonged pause (~ 2 s). Converging-eye movements were generally seen but not always during prey-capture maneuvers.

Both the *paramecia*-larva distances, d_{param}, and relative angles (**Figure 7C**) at the moment of detection were measured relative to the eyes' longitudinal axis, from the point described roughly by the intersection of the larva's midline, with the line that connects both eyes' centroids. Then, d_{param} was converted to angular size of *paramecia* on the larva's retina at the moment of detection, α_{param} (**Figure 7E**), as:

$$\alpha_{param} = 2 \cdot \tan^{-1}\left(l_{param} / 2\, d_{param}\right) \qquad (11)$$

Where l_{param} is the typical size of a *paramecium* (~200 µm). Given the size of the wells and that of the *paramecia*, the minimal theoretical possible α_{param} value was 0.7°. The typical d_{param} that we obtained ($d_{param} = 1.9 \pm 0.86$ mm) and the angular distribution of prey-detection events (**Figure 7C**) were both in close agreement with previous reports (Bianco et al., 2011; McElligott and O’malley, 2005).

SUPPLEMENTAL REFERENCES

Aggarwal, C., Hinneburg, A., and Keim, D. (2001). On the surprising behavior of distance metrics in high dimensional space. In ICDT '01 Proceedings of the 8th International Conference on Database Theory, (London: Springer-Verlag), pp. 420–434.

Akerboom, J., Chen, T.-W., Wardill, T.J., Tian, L., Marvin, J.S., Mutlu, S., Calderón, N.C., Esposti, F., Borghuis, B.G., Sun, X.R., et al. (2012). Optimization of a GCaMP calcium indicator for neural activity imaging. J. Neurosci. *32*, 13819–13840.

Bathellier, B., Ushakova, L., and Rumpel, S. (2012). Discrete neocortical dynamics predict behavioral categorization of sounds. Neuron *76*, 435–449.

Bianco, I.H., Kampff, A.R., and Engert, F. (2011). Prey capture behavior evoked by simple visual stimuli in larval zebrafish. Front. Syst. Neurosci. *5*, 101.

Brainard, D.H. (1997). The Psychophysics Toolbox. Spat. Vis. *10*, 433–436.

Burrill, J.D., and Easter, S.S. (1994). Development of the retinofugal projections in the embryonic and larval zebrafish (Brachydanio rerio). J. Comp. Neurol. *346*, 583–600.

Davies, D.L., and Bouldin, D.W. (1979). A Cluster Separation Measure. IEEE Trans. Pattern Anal. Mach. Intell. *PAMI-1*, 224–227.

Dayan, P., and Abbott, L.F. (2001). Theoretical Neuroscience: Computational and Mathematical Modeling of Neural Systems (Cambridge: The MIT Press).

Dombeck, D. a, Khabbaz, A.N., Collman, F., Adelman, T.L., and Tank, D.W. (2007). Imaging large-scale neural activity with cellular resolution in awake, mobile mice. Neuron *56*, 43–57.

Gonzalez, R.C., and Woods, R.E. (2009). Digital Image Processing (3rd Edition) (Gatesmark Publishing).

Hendrickson, A.E., and White, P.O. (1964). Promax: a quick method for rotation to oblique simple structure. Br. J. Stat. Psychol. *17*, 65–70.

Hilgetag, C., Kötter, R., Stephan, K., and Sporns, O. (2002). Computational methods for the analysis of brain connectivity. In Computational Neuroanatomy–Principles and Methods, G. Ascoli, ed. (Totowa: Humana Press), pp. 295–335.

Kruskal, J.B., and Wish, M. (1978). Multidimensional Scaling (Beverly Hills, California: SAGE).

Lister, J.A., Robertson, C.P., Lepage, T., Johnson, S.L., and Raible, D.W. (1999). nacre encodes a zebrafish microphthalmia-related protein that regulates neural-crest-derived pigment cell fate. Development *126*, 3757–3767.

Lopes-dos-Santos, V., Conde-Ocazionez, S., Nicolelis, M. a L., Ribeiro, S.T., and Tort, A.B.L. (2011). Neuronal assembly detection and cell membership specification by principal component analysis. PLoS One *6*, e20996.

McElligott, M.B., and O'malley, D.M. (2005). Prey tracking by larval zebrafish: axial kinematics and visual control. Brain. Behav. Evol. *66*, 177–196.

Niell, C.M., and Smith, S.J. (2005). Functional imaging reveals rapid development of visual response properties in the zebrafish tectum. Neuron *45*, 941–951.

Panier, T., Romano, S.A., Olive, R., Pietri, T., Sumbre, G., Candelier, R., and Debrégeas, G. (2013). Fast functional imaging of multiple brain regions in intact zebrafish larvae using Selective Plane Illumination Microscopy. Front. Neural Circuits *7*, 65.

Park, H.C., Kim, C.H., Bae, Y.K., Yeo, S.Y., Kim, S.H., Hong, S.K., Shin, J., Yoo, K.W., Hibi, M., Hirano, T., et al. (2000). Analysis of upstream elements in the HuC promoter leads to the establishment of transgenic zebrafish with fluorescent neurons. Dev. Biol. *227*, 279–293.

Pelli, D.G. (1997). The VideoToolbox software for visual psychophysics: transforming numbers into movies. Spat. Vis. *10*, 437–442.

Peyrache, A., Benchenane, K., Khamassi, M., Wiener, S.I., and Battaglia, F.P. (2010). Principal component analysis of ensemble recordings reveals cell assemblies at high temporal resolution. J. Comput. Neurosci. *29*, 309–325.

Pologruto, T.A., Sabatini, B.L., and Svoboda, K. (2003). ScanImage: flexible software for operating laser scanning microscopes. Biomed. Eng. Online *2*, 13.

Sporns, O., Honey, C., and Kötter, R. (2007). Identification and classification of hubs in brain networks. PLoS One.

Stuermer, C.A. (1988). Retinotopic organization of the developing retinotectal projection in the zebrafish embryo. J. Neurosci. *8*, 4513–4530.

Theodoridis, S., and Koutroumbas, K. (2009). Pattern Recognition.

Tian, L., Hires, S.A., Mao, T., Huber, D., Chiappe, M.E., Chalasani, S.H., Petreanu, L., Akerboom, J., McKinney, S. a, Schreiter, E.R., et al. (2009). Imaging neural activity in worms, flies and mice with improved GCaMP calcium indicators. Nat. Methods *6*, 875–881.

Tibshirani, R., Walther, G., and Hastie, T. (2001). Estimating the number of clusters in a data set via the gap statistic. J. R. Stat. Soc. Ser. B (Statistical Methodol. *63*, 411–423.

Tracy, C.A., and Widom, H. (1992). Level-Spacing Distributions and the Airy Kernel. Commun. Math. Phys. *159*, 35.

Tseng, Q., Duchemin-Pelletier, E., Deshiere, A., Balland, M., Guillou, H., Filhol, O., and Théry, M. (2012). Spatial organization of the extracellular matrix regulates cell-cell junction positioning. Proc. Natl. Acad. Sci. U. S. A. *109*, 1506–1511.

Tsodyks, M., Kenet, T., Grinvald, A., and Arieli, A. (1999). Linking Spontaneous Activity of Single Cortical Neurons and the Underlying Functional Architecture. Science (80-.). *286*, 1943–1946.

Westerfield, M. (2007). The zebrafish book: a guide for the laboratory use of zebrafish (Danio rerio) (Eugene, Oregon: University of Oregon Press).

Yamada, Y., Michikawa, T., Hashimoto, M., Horikawa, K., Nagai, T., Miyawaki, A., Häusser, M., and Mikoshiba, K. (2011). Quantitative comparison of genetically encoded Ca indicators in cortical pyramidal cells and cerebellar Purkinje cells. Front. Cell. Neurosci. *5*, 18.